THE ASTRONOMICAL JOURNAL VOLUME 105, NUMBER 5 MAY 1993

# VERY LARGE ARRAY IMAGING OF FIVE FANAROFF–RILEY II 3CR RADIO GALAXIES

ILIAS FERNINI AND JACK O. BURNS

Department of Astronomy, New Mexico State University, Las Cruces, New Mexico 88003
Electronic mail: jburns@nmsu.edu

ALAN H. BRIDLE

National Radio Astronomy Observatory,[1] 520 Edgemont Road, Charlottesville, Virginia 22903-2475
Electronic mail: abridle@nrao.edu

RICK A. PERLEY

National Radio Astronomy Observatory,[1] P.O. Box O, Socorro, New Mexico 87801
Electronic mail: rperley@aoc.nrao.edu

*Received 1992 November 17; revised 1992 December 29*

## ABSTRACT

This paper presents high resolution, high dynamic range Very Large Array (VLA) radio images of five luminous classical double radio galaxies (RGs) at 5 GHz. We detect the radio cores of at least four of these RGs. A long, continuous radio jet is seen only in one source, 3C 22, in contrast to the 100% jet detection in a comparable sample of QSRs. However, there are candidate jets or jet components seen in three other RGs. Overall, the jets in these RGs are less prominent, relative to the lobes, than those in the quasar sample. We also compare the polarization properties of these RGs at three different wavelengths: 3.6, 6, and 20 cm. Moderate depolarization asymmetries between 6 and 20 cm are found between the lobes of two RGs, 3C 22 and 3C 324. Finally, we compare our VLA maps with optical [O II] images in search of correlations between radio properties and emission line asymmetries. These data will be used to test the RG/QSR unification scheme of Barthel [ApJ, 336, 606 (1989)].

## 1. INTRODUCTION

This paper is the first of a series that reports on a search for jets and counterjets in powerful extended radio galaxies (FR class II sources—Fanaroff & Riley 1974). This search was motivated by schemes that have been proposed to unify radio-loud FRII quasars and FRII radio galaxies as members of the same parent AGN population observed in systematically different orientations to the line of sight (e.g., Bridle & Perley 1984; Barthel 1989). In particular, Barthel suggested that all extended radio sources with powers $P_{178} \geqslant 10^{27}$ W Hz$^{-1}$ contain similar jets with bulk relativistic velocities ($\gamma > 2$) but that the optical appearance of their parent objects depends on their orientation relative to the observer. He proposed that a bright optical continuum and a broad-line region are common to all the parent objects, but are hidden by an obscuring dust torus if the radio jets are oriented near the plane of the sky. AGNs in this orientation would therefore be classified as narrow-line radio galaxies. At the other extreme, if the axis of the radio jets is near the line of sight, the strong continuum and broad lines would not be obscured, and the same source would be classified as a radio-loud quasar. (Intermediate cases might be described either as quasars or as broad-line radio galaxies.) In Barthel's model, the parent population of intrinsically similar AGNs is randomly oriented, and the transition from radio-galaxy to quasar properties should occur around 44° to the line of sight.

The apparent flux densities of relativistic jets also depend strongly on their orientation relative to the observer because of beaming effects (e.g., Blandford & Königl 1979). The extended lobe emission should not be beamed significantly, however, as most models of the lobes imply that bulk motions within them will be subrelativistic and that the pitch angles of the relativistic electron motions will be randomized relative to the magnetic fields. The *prominence* of the jets relative to the lobes (measured by the ratio of their integrated flux densities) may therefore be an indicator of the importance of beaming in any sample of FRII sources.

Unified models of FRII sources, such as Barthel's, predict systematic differences between the prominence, relative to the lobes, of the jets and counterjets in quasars and radio galaxies. In the quasars, the emission from the (approaching) jet would be beamed towards the observer and that from the (receding) counterjet would be beamed away. In FRII radio galaxies, whose jets should be systematically nearer to the plane of the sky, the emission of neither jet should be strongly beamed towards the observer. (Indeed, for galaxies whose jets are close to the plane of the sky, relativistic beaming may make both jets apparently fainter than they would appear if their velocities were nonrelativistic.) FRII quasars should therefore tend to have jets that are more prominent relative to their

[1]The National Radio Astronomy Observatory is operated by Associated Universities, Inc., under cooperative agreement with the National Science Foundation.

 0004-6256/93/051690-20$00.90 

lobes than those in the radio galaxies (whose jets are known to be hard to detect, e.g., Perley *et al.* 1984). The *counter*jets should, however, be easier to detect in the radio galaxies, and the jet/counterjet ratios should be systematically higher in quasars than in radio galaxies. The *relative prominence* (integrated flux density ratios) of jets, counterjets, and lobes in extended radio galaxies and quasars can therefore provide several good tests for unified schemes such as Barthel's if relativistic beaming effects are dominant (see, also, Bridle 1992).

A second type of test for such unified schemes may be provided by the systematically asymmetric depolarization of the lobes of FRII sources that was discovered by Laing (1988) and by Garrington *et al.* (1988, 1991). These authors found, in samples dominated by quasars, that the lobe on the side of the brighter jet systematically depolarizes at a longer wavelength than the other lobe. They suggested that the depolarization asymmetry could depend on orientation, if it arises from unresolved structure in a Faraday-thick magnetoionic medium that surrounds the typical FRII source. According to the unified schemes, the lobe that is fed by the brighter jet would also be closer to the observer. This lobe would be viewed along a shorter path through the magnetoionic medium, and would therefore depolarize at a longer wavelength than the other lobe. If the jets in FRII quasars are indeed oriented nearer to the lines of sight than those in FRII radio galaxies, and all AGNs are surrounded by similar media, we should expect to find greater depolarization asymmetries in the quasars than in the radio galaxies.

This series of papers seeks to test the unified schemes using data on jet and counterjet prominence and on depolarization asymmetries from sensitive, high resolution VLA imaging and polarimetry of samples of FRII radio galaxies and quasars. The importance of high-quality imaging for such work was demonstrated by preliminary results (reported in Bridle 1990) of a study of a sample of twelve extended 3CR quasars (Bridle *et al.* 1993). This study showed that fully-sampled VLA syntheses detected the brighter jets in 100% of the 3CR quasar sample, and found faint counterjet candidates in about half of them. The status of these quasar counterjet candidates is ambiguous, however. Most are discontinuous, and none occurs opposite an uninterrupted straight segment of the main jet. These properties suggest that interactions and perturbations of the quasar jets play an important role in determining their visibility. The quasar study also emphasized the difficulty of distinguishing faint jets and counterjets from filaments in the lobes of FRII sources. High-quality images are clearly crucial to any attempt to test unified schemes using jet and counterjet prominence statistics. We have therefore sought to obtain images that will let us exclude "twisted or broken" regions of jets that may have interacted strongly with their environments, and that may distinguish jets and counterjets from other curvilinear fine structure in the lobes.

This paper defines a sample of 13 FRII 3CR radio galaxies whose properties we wish to compare with those of the sample of 13 FRII 3CR quasars obtained by combining the Bridle *et al.* (1993) quasar sample with the study of 3C 47 by Fernini *et al.* (1991). It presents results on the first 5 of these 13 radio galaxies to be observed in an ongoing program of sensitive, high resolution VLA imaging at 1.4, 5, and 8.4 GHz.

Section 2 describes the selection of the radio galaxies and Sec. 3 discusses the VLA observing and imaging techniques. Section 4 describes each source individually. Section 5 presents an analysis of the depolarization asymmetry between the radio lobes. Section 6 examines the jet and optical emission line asymmetries of the RGs. Section 7 discusses and summarizes the results of these first observations of our sample of 3CR classical double radio galaxies.

Throughout this paper, we use $H_0=75$ km/s/Mpc, $q_0=0.5$, we assume a Friedmann–Robertson cosmology, and we quote sky positions in epoch B1950.

## 2. SOURCE SELECTION

### *2.1 Sample of Radio Galaxies*

Our sample of 3CR radio galaxies was originally selected to match the criteria in the quasar sample of Bridle *et al.* (1993); i.e., an unbiased sample of sources stronger than 10 Jy at 178 MHz and $>10''$ in angular extent. Our objective was to have two statistically similar samples in terms of redshift, luminosity, and size so that both samples can be compared in terms of the jet/counterjet flux density ratios.

The sample of 3CR radio galaxies was drawn from two main catalogues: (i) the third Cambridge catalogue of radio sources (Spinrad *et al.*, 1985) which contains about 216 radio galaxies, and (ii) the complete sample of Laing *et al.* (1983) which lists radio sources with $S_{178\ \mathrm{MHz}}>10$ Jy. The full selection criteria that we used are as follows.

(1) Declination: $20°\leqslant\delta<70°$. This criterion was necessary first to have the best possible $(u,v)$ coverage for our sources. It also reduced the number of candidate radio galaxies from 216 to 121 sources. This range of declinations is close to that of the quasar sample.

(2) Redshift: $0.3<z<1.4$. Except for 3C 9, the RG and quasar samples are all inside this range. This further reduced the sample to 43 sources.

(3) Flux density: $S_{178\ \mathrm{MHz}}>10$ Jy. This criterion helps to ensure that sufficient component flux density will be available when the sources are well resolved by the VLA. With this criterion, 9 more sources were eliminated.

(4) Largest angular size: $10''\leqslant\mathrm{LAS}<100''$. The lower limit was set so that the two radio lobes will not be confused with any jet structure if it exists given the $\sim0''.35$ resolution of the VLA at 5 GHz. The upper limit allows us to conveniently image the radio source with the type of VLA configuration (and field of view) used. The sample now contains 26 sources.

### *2.2 The Observed Radio Galaxy Sample*

This paper presents the results of the first of two rounds of VLA observations allocated to this project, in which we observed the five radio galaxies shown in bold type in Table 1. In the second VLA observing round, eight more sources

TABLE 1. Sample of 3CR radio galaxies.

| SOURCE | $\alpha$(1950) $\delta$(1950) | z | LAS (″) | l (kpc) | $S_{5GHz}$ (Jy) | $\log(L_{5GHz})$ (W/Hz) |
|---|---|---|---|---|---|---|
| 3C 20.0 | 00 40 20.00 51 47 08.1 | 0.350 | 51 | 204 | 4.18 | 27.0 |
| **3C 22** | **00 48 04.73 50 55 44.8** | **0.937** | **24** | **135** | **0.76** | **27.2** |
| 3C 34.0 | 01 07 32.58 31 31 22.5 | 0.689 | 48 | 254 | 0.43 | 26.7 |
| 3C 42.0 | 01 25 42.67 28 47 30.4 | 0.395 | 28 | 119 | 0.84 | 26.4 |
| **3C 55** | **01 54 19.03 28 37 00.6** | **0.7348** | **69** | **372** | **0.88** | **27.05** |
| 3C 244.1 | 10 30 19.61 58 30 04.3 | 0.428 | 51 | 226 | 1.12 | 26.7 |
| 3C 252.0 | 11 08 48.84 35 56 59.8 | 1.1035 | 57 | 326 | 0.32 | 27.1 |
| **3C 265** | **11 42 52.0 31 50 29.1** | **0.811** | **78** | **429** | **0.63** | **27.0** |
| **3C 324** | **15 47 37.3 21 34 42.** | **1.2063** | **10** | **57** | **0.61** | **27.4** |
| 3C 325 | 15 49 13.98 62 50 21.3 | 0.86 | 16 | 89 | 0.83 | 27.2 |
| 3C 330.0 | 16 09 13.90 66 04 22.8 | 0.550 | 56 | 276 | 2.35 | 27.2 |
| **3C 356** | **17 23 06.96 51 00 14.1** | **1.079** | **75** | **429** | **0.38** | **27.07** |
| 3C 441 | 22 03 49.27 29 14 43.8 | 0.707 | 29 | 155 | 0.92 | 27.0 |

were observed. In total, we observed 13 radio galaxies out of a sample of 26 that were well-matched with the assigned VLA observing time blocks. In these first observations, all five sources were observed at 1.4, 5, and 8.4 GHz. Some earlier observations of the sources at these frequencies have also been provided by their observers. Table 2 lists the subsample of radio galaxies along with the date of observation, the array configuration, the frequency, the bandwidth, the integration time, and the name of the observer.

The sample of RGs in Table 1 has distributions of redshifts and luminosities which are statistically indistinguishable (using a Kolmogorov–Smirnov test) from those of the QSRs in the Bridle *et al.* (1993) sample. However, the average angular size of the RGs for the subsample of 13 (34″) is somewhat less that that of the QSR sample (43″). These properties will be discussed in more detail when radio imaging of the larger RG sample is completed.

TABLE 2. Observed sample of 3CR radio galaxies.

| Source | Date | Config. | Freq (GHz) | Bandw. (MHz) | Int.Time (min.) | Observer |
|---|---|---|---|---|---|---|
| 3C 22 | 22/04/90 | A | 5.0 | 50 | 200 | Fernini |
| | 12/08/90 | B | 8.4 | 50 | 53 | Fernini |
| | 16/09/90 | B | 5.0 | 50 | 132 | Fernini |
| | 16/09/90 | B | 1.4 | 50 | 41 | Fernini |
| 3C 55 | 22/04/90 | A | 5.0 | 25 | 200 | Fernini |
| | 12/08/90 | B | 8.4 | 50 | 46 | Fernini |
| | 16/09/90 | B | 5.0 | 25 | 128 | Fernini |
| | 07/12/86 | B | 1.4 | 25 | 35 | Leahy |
| 3C 265 | 22/04/90 | A | 5.0 | 25 | 190 | Fernini |
| | 16/09/90 | B | 8.4 | 50 | 55 | Fernini |
| | 12/14/87 | B | 5.0 | 25 | 240 | McCarthy |
| | 16/09/90 | B | 1.4 | 50 | 41 | Fernini |
| 3C 324 | 22/04/90 | A | 5.0 | 50 | 180 | Fernini |
| | 31/08/90 | B | 8.4 | 50 | 40 | Fernini |
| | 16/09/90 | B | 5.0 | 50 | 132 | Fernini |
| | 16/09/90 | B | 1.4 | 50 | 42 | Fernini |
| 3C 356 | 22/04/90 | A | 5.0 | 25 | 200 | Fernini |
| | 16/09/90 | B | 8.4 | 50 | 44 | Fernini |
| | 16/09/90 | B | 5.0 | 25 | 130 | Fernini |
| | 07/13/86 | B | 1.4 | 50 | 21 | Leahy |

TABLE 3. (a) Calibrators used in the 6 cm A and B configuration observations.

| Source | Calibrator | $\alpha$(1950) hh mm ss.ss | $\delta$(1950) dd mm ss.s | Flux density (Jy) |
|---|---|---|---|---|
| 3C 22 | 0026+346 | 00 26 34.83 | 34 39 57.7 | 1.85 |
| 3C 55 | 0202+319 | 02 02 09.65 | 31 58 10.4 | 1.47 |
| | 0026+346 | 00 26 34.83 | 34 39 57.7 | 1.85 |
| 3C 265 | 1144+402 | 11 44 21.02 | 40 15 14.2 | 1.30 |
| 3C 324 | 1600+335 | 16 00 11.91 | 33 35 09.6 | 2.00 |
| | 1611+343 | 16 11 47.9 | 34 20 19.8 | 2.30 |
| 3C 356 | 1739+522 | 17 39 29.0 | 52 13 10.4 | 0.90 |
| | 1611+343 | 16 11 47.9 | 34 20 19.8 | 2.30 |
| 3C 286 | 1328+307 | 13 28 49.65 | 30 45 58.6 | 7.4 |

(b) Calibrators used in the 3.6 cm B configuration observations.

| Source | Calibrator | $\alpha$(1950) hh mm ss.ss | $\delta$(1950) dd mm ss.s | Flux density (Jy) |
|---|---|---|---|---|
| 3C 22 | 0224+671 | 02 24 41.17 | 67 07 39.7 | 2.12 |
| 3C 55 | 0133+476 | 01 33 55.10 | 47 36 12.8 | 1.80 |
| 3C 265 | 0955+476 | 09 55 08.53 | 47 39 28.2 | 0.84 |
| 3C 324 | 1624+416 | 16 24 18.25 | 41 41 23.5 | 1.03 |
| 3C 356 | 1738+476 | 17 38 36.31 | 47 39 28.7 | 0.94 |
| 3C 286 | 1328+307 | 13 28 49.65 | 30 45 58.6 | 5.2 |

(c) Calibrators used in the 20 cm B configuration observations.

| Source | Calibrator | $\alpha$(1950) hh mm ss.ss | $\delta$(1950) dd mm ss.s | Flux density (Jy) |
|---|---|---|---|---|
| 3C 22 | 0026+346 | 00 26 34.83 | 34 39 57.7 | 1.85 |
| 3C 265 | 0953+254 | 09 53 59.7 | 25 29 33.6 | 0.90 |
| 3C 324 | 1611+343 | 16 11 47.9 | 34 20 19.8 | 2.70 |
| 3C 286 | 1328+307 | 13 28 49.65 | 30 45 58.6 | 14.70 |

## 3. OBSERVING AND IMAGING TECHNIQUES

To detect low surface brightness emission yet still distinguish jets from other features, we have sought the highest dynamic range and good angular resolution. To achieve the necessary combinations, we:

(i) observed the sample in the VLA A and B configurations at 5 GHz using the long total integration times noted in Table 2. The two data bases were then added together. A final resolution of $\sim$0″.35 was obtained.

(ii) acquired well-sampled $(u,v)$ coverage by observing at many hour angles spread over the length of time the source was above the horizon.

(iii) used the bandwidths listed in Table 2. These bandwidths were chosen to maximize sensitivity while limiting the distortions produced by chromatic aberration (e.g., Cotton 1989) at the outer edges of the lobes to $<5\%$ (as measured by the intensity reduction for a point source).

This strategy was applied to all observing runs allocated to this project. Unlike the 5 GHz observations, the 1.4 and 8.4 GHz observations were made only in the B configuration. At 1.4 GHz, two sources (3C 55 and 3C 356) were

TABLE 4. (a) RMS noises and dynamic ranges for the 6 cm maps.

| | 3C 22 | 3C 55 | 3C 265 | 3C 324 | 3C 356 |
|---|---|---|---|---|---|
| I image (rms/beam) | 30(22) | 22(20) | 24(20) | 30(22) | 25(20) |
| Q, U images (rms/beam) | 27 | 28 | 32 | 32 | 32 |
| Dynamic Range | 5600:1 | 2800:1 | 3500:1 | 4500:1 | 1250:1 |

Note to TABLE 4a.

Flux densities are in $\mu$Jy.

(b) RMS noises and dynamic ranges for the 3.6 cm maps.

| | 3C 22 | 3C 55 | 3C 265 | 3C 324 | 3C 356 |
|---|---|---|---|---|---|
| I image (rms/beam) | 50(30) | 15(15) | 17(15) | 40(25) | 24(20) |
| Q, U images (rms/beam) | 31 | 25 | 31 | 27 | 35 |
| Dynamic Range | 2700:1 | 3700:1 | 4000:1 | 3000:1 | 1050:1 |

Note to Table 4b.

Flux densities are in $\mu$Jy.

(c) RMS noises and dynamic ranges for the 20 cm maps.

| | 3C 22 | 3C 55 | 3C 265 | 3C 324 | 3C 356 |
|---|---|---|---|---|---|
| I image (rms/beam) | 0.3(0.1) | 0.6(0.1) | 0.35(0.1) | 0.65(0.2) | 0.4(0.1) |
| Q, U images (rms/beam) | 0.09 | 0.14 | 0.13 | 0.2 | 0.08 |
| Dynamic Range | 1900:1 | 1250:1 | 3300:1 | 2300: 1 | 1600:1 |

Note to TABLE 4c.

Flux densities are in mJy.

previously observed by Patrick Leahy who kindly provided his data to us. For all the observations, the primary flux density and polarization position angle calibrator was 3C 286 which we assumed to have flux densities of 14.5, 7.4, and 5.2 Jy at 1.4, 4.9, and 8.4 GHz, respectively, and a polarization position angle of 66° at all frequencies. The resulting flux density scale is that of Baars *et al.* (1977).

Table 2 lists the total integration times and bandwidths for the five sources. Table 3(a) lists the primary and secondary flux density calibrators used in the 5 GHz observations along with their flux densities and their positions. Tables 3(b) and 3(c) list the secondary calibrators used in the 8.4 and 1.4 GHz observations, respectively.

The A and B configuration data were calibrated following standard procedures (e.g., Fomalont & Perley 1989) using the NRAO AIPS software. For the 20 cm data, ionospheric Faraday rotation introduces significant errors into the apparent E-vector position angles. The ionospheric rotation at 20 cm was corrected, using a model based on observed electron densities, with the AIPS task FARAD.

After the external calibrations, the data were Fourier transformed and deconvolved to obtain CLEANed images of the three Stokes parameters *I*, *Q*, and *U* using the ungridded-subtraction algorithm in the AIPS task MX. These initial clean components served as input models for the self-calibration using the AIPS task ASCAL (Schwab 1980) to correct for atmospheric, system phase, and amplitude variations.

Table 4 lists the parameters of the final images. The theoretical noise is given in parentheses beside the measured rms noise. At 3.6 and 6 cm, the rms noises on the final images were mostly within 25% of the theoretical noise limits. At 20 cm, the images are limited by confusion rather than by thermal noise. A greyscale mosaic of these RG images is shown in Fig. 1 (Plate 84). Contour maps of these radio galaxies are presented in Figs. 2–6.

## 4. THE IMAGES

### *4.1 Terminology*

The terms *core, jet, lobe*, and *hot spot* require careful definitions if they are to be used precisely in describing features seen on high resolution, high dynamic range VLA images. For consistency, we use the definitions proposed by Bridle *et al.* (1993) which we summarize as follows.

**(1) Core**—a central unresolved feature coinciding to within observational errors with the best available position for the optical galaxy.

**(2) Jet**—a narrow feature that is (a) at least four times as long as it is wide (after deconvolving the synthesized beam), (b) separable at high resolution from other extended structure either spatially or by brightness contrast, and (c) aligned with the nucleus of the parent object where it is closest to it. Many jets contain compact brightness enhancements that we will term "jet knots."

**(3) Lobes**—features which contain all of the other radio emission produced by the source excluding (1) and (2).

**(4) Hot Spot**—if no jet is detected, a feature that (a) is the brightest structure in the lobe, (b) has surface brightness more than four times that of the surrounding emission, and (c) has a linear FWHM (after deconvolving the synthesized beam) that is $< 5\%$ of the largest diameter of the source. If a jet is detected, the hot spot must additionally be further from the nucleus than the end of the jet, which is defined by (1) its disappearance, or (2) an abrupt change in direction by at least 30°, or (3) decollimation by more than a factor of two.

The hot spot definition is intended to isolate a class of compact, bright, feature that marks a major change in the apparent direction and/or collimation of a jet, whether or not the jet itself is detectable. Where a jet is detected, the definition seeks to distinguish hot spots from the jet knots that may be only minor disturbances in an ongoing flow.

### *4.2 Discussion of Individual Sources*

#### *4.2.1 3C 22*

Jenkins *et al.* (1977) first resolved 3C 22 using the Cambridge 5 km telescope with 2".5 FWHM at 5 GHz. Their map showed two small extended lobes separated by about 24". A 5 GHz VLA observation by Schilizzi *et al.* (1982) at 1" resolution revealed two components with unresolved features at the outer edges of the source. No core or jet was detected.

Figure 2(a) shows contours of total intensity at 0".35 resolution. Several significant new features can be seen. A

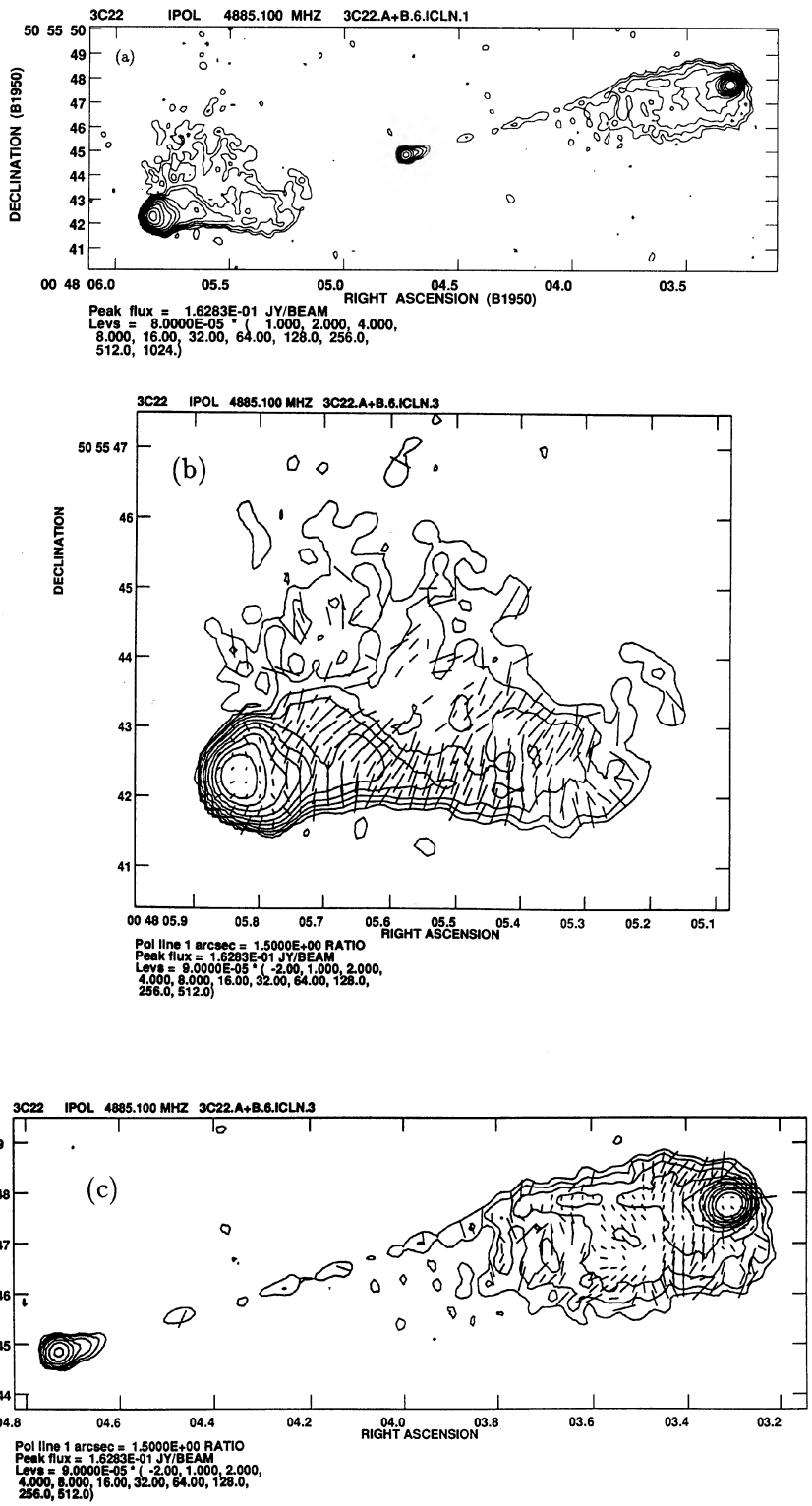


FIG. 2. (a) 6 cm total intensity map of 3C 22 at 0.″35 resolution from the combined A and B configuration data. (b) Enlargement of the SE lobe of 3C 22 and its distribution of the $E$ vectors of the linear polarization at 5 GHz. (c) Enlargement of the NW lobe of 3C 22 and its distribution of the $E$ vectors of the linear polarization at 5 GHz. (d) Contour map of the total intensity of 3C 22 at 3.6 cm at 0.″67 resolution with polarization $E$ vectors overlaid. The contours levels are $-2$, 1, 2, 4, 8, 16,..., 128, and 256 times 0.15 mJy per CLEAN beam area. The peak flux density is $1.36\times10^{-1}$ Jy/beam. The $E$-vector scale is such that a vector length of 1 arcsec corresponds to $p=0.65$. (e) Contour map of the total intensity of 3C 22 at 20 cm at 3.″85 resolution with polarization $E$ vectors overlaid. The contours levels are $-2$, 1, 2, 4, 8, 16,..., 128, and 256 times 0.9 mJy per CLEAN beam area. The peak flux density is $5.74\times10^{-1}$ Jy/beam. The $E$-vector scale is such that a vector length of 1 arcsec corresponds to $p=0.12$.

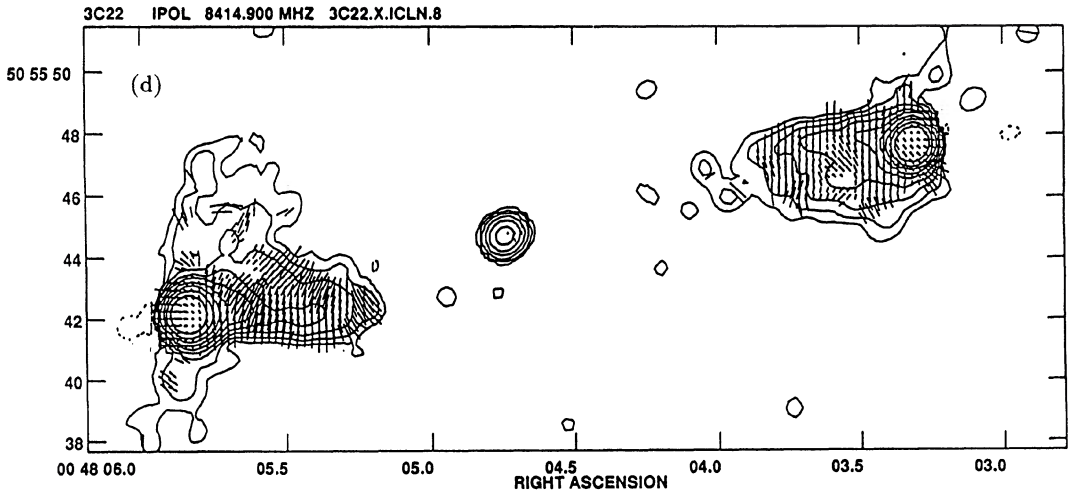


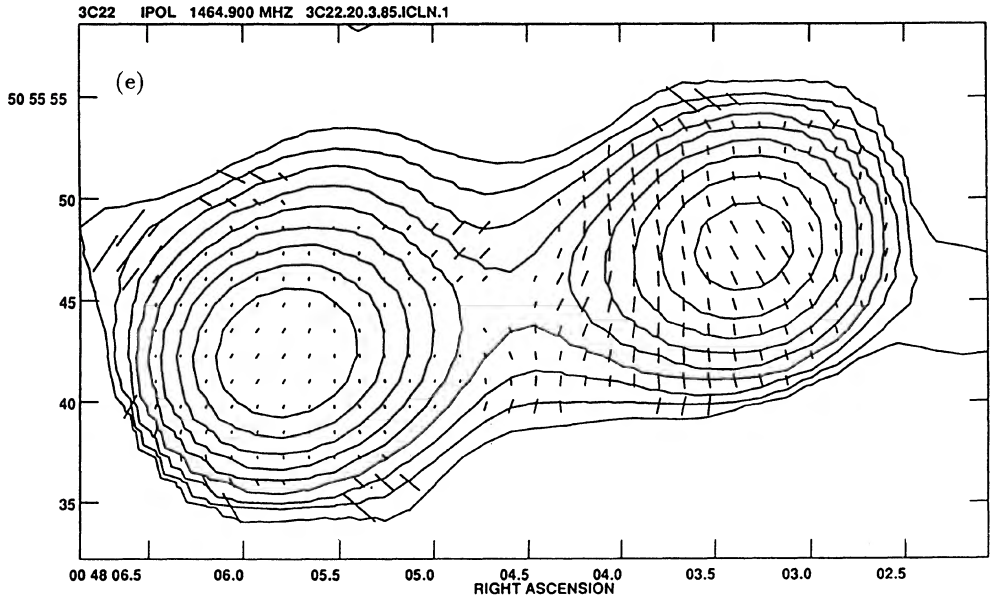


FIG. 2. (continued)

compact core is now visible between the two extended lobes. Its peak is located at $\alpha = 00^h48^m04^s731$ and $\delta = 50°55'44''.84$. The optical identification proposed by Spinrad *et al.* (1985) coincides with this position to within 0".1. We therefore consider this identification to be confirmed. The radio properties of the 3C 22 core and those of the other RGs are listed in Table 5. Sizes have been measured by fitting two-dimensional (2-D) elliptical Gaussian models (deconvolved from the synthesized beam) using the AIPS task IMFIT. Note that the core of 3C 22 is slightly resolved.

TABLE 5. Core deconvolved sizes, flux densities, and powers.

| Source | Size (max × min, p.a.) | Total $S_5$ (mJy) | $P_5$ (W/Hz) |
|---|---|---|---|
| 3C 22 | 0".09 × 0".03, 109° | 7.83 | $1.71 \times 10^{25}$ |
| 3C 55 | 0".06 × 0".03, 138° | 5.32 | $7.26 \times 10^{24}$ |
| 3C 265 | < 0".12 | 2.62 | $4.24 \times 10^{24}$ |
| 3C 356 D | < 0".13 | 1.07 | $3.37 \times 10^{24}$ |
| E | < 0".20 | 0.54 | $1.70 \times 10^{24}$ |

A further new feature is the faint jet which links the core and the NW lobe. This jet is best seen in the greyscale image of 3C 22 in Fig. 1. It is straight for about 10".6 (60 kpc), then bends by about 5° with respect to its initial direction. The curved jet can be traced for a further 2".4 (13 kpc) until it blends into the NW lobe.

TABLE 6. Lobe feature sizes, core/lobe-feature distances, and lobe flux densities at 5 GHz.

| Deconvolved FWHM | Distances | Lobe $S_5$ (mJy) |
|---|---|---|
| | **3C 22** | |
| NW | Core - NW HS | NW lobe |
| 0″.40 × 0″.31 | 14″.6 (82.5 kpc) | 260 |
| SE | Core - SE HS | SE lobe |
| 0″.47 × 0″.32, −77° | 11″.4 (64.4 kpc) | 361 |
| | **3C 55** | |
| Feature F2 | Core - Feature F2 | |
| 0″.25 × 0″.18, 27° | 12″.5 (67.2 kpc) | |
| Feature F6 | Core - Feature F6 | |
| 0″.31 × 0″.24, 50° | 16″.0 (86.0 kpc) | |
| Feature F8 | Core - Feature F8 | SE lobe |
| 0″.65 × 0″.56, 139° | 35″ (188.2 kpc) | 236 |
| NW HS | Core - NW HS | NW lobe |
| 0″.72 × 0″.35 | 36″ (194 kpc) | 247 |
| | **3C 265** | |
| Feature A | Core - Feature A | NW lobe |
| 1″.22 × 0″.73, 0° | 46″.7 (256.9 kpc) | 286 |
| Feature C | | SE lobe |
| 0″.69 × 0″.41, 178° | | 387 |
| Feature E | Core - Feature E | |
| 0″.69 × 0″.41, 0° | 30″ (165 kpc) | |
| | **3C 324** | |
| Feature A | | SW lobe |
| 0″.46 × 0″.33 | — | 128 |
| Feature E | | NE lobe |
| 0″.48 × 0″.33, −30° | — | 512 |
| | **3C 356** | |
| Feature A | Feature D - Feature A | NW lobe |
| 0″.81 × 0″.38 | 50″ (286 kpc) | 134 |
| Feature B | | SE lobe |
| 0″.60 × 0″.38 | | 182 |
| Feature C | | |
| 0″.64 × 0″.38 | | |
| Feature F | Feature D - Feature F | |
| 0″.64 × 0″.38 | 25″ (143 kpc) | |

Both lobes have diffuse emission extending back toward the core (Fig. 1). The east lobe has a bright curved tail that could either be part of a possible "counterjet" or a bright filament on the boundary of the lobe, as commonly found in other radio galaxies (e.g., Cygnus A in Perley *et al.* 1984). Neither the main jet nor the "possible counterjet" are on the axis that passes through the eastern hot spot, the core, and the western hot spot. These three features are aligned to within 2°, but the straight segment of the main jet is 5° northward of this axis, and parts of the curved, narrow feature are about 10° southward of it.

Although the two hot spots are fairly well aligned along the radio source axis, they are not symmetric in compactness. Their sizes were also estimated by fitting 2-D elliptical Gaussian models. Table 6 gives the fitted hot spot sizes, together with the core/lobe-feature distances and the lobe flux densities at 5 GHz. The hot spot in the jetted (NW) lobe is the more compact, as is commonly found in other powerful radio sources with asymmetric jets (e.g., Laing 1989).

Figure 2(b) shows the SE lobe and Fig. 2(c) shows the core, jet, and NW lobe. Polarization $E$ vectors are overlaid onto the intensity contours where the vector lengths in these and the other source maps are proportional to the fractional polarization. For the composite $I$-$p$-$\chi$ maps, we truncated below a signal-to-noise ratio of 4 in all polarization maps in this paper. The jet is weakly polarized ($<4\%$), while the "possible counterjet" feature shows $\sim 20\%$ polarization with the $E$ vectors perpendicular to the feature over much of its length. This degree of polarization and $E$-vector orientation are also typical of lobe boundary features and filaments in radio galaxies, so they do not help us to decide whether this feature is part of a counterjet.

Figures 2(d) and 2(e) show contour maps of the total intensity of 3C 22 at 3.6 and 20 cm, respectively, with polarization $E$ vectors overlaid. The resolutions are 0″.67 and 3″.85 for the 3.6 and 20 cm maps, respectively. The 3.6 cm map reveals the core, but not the jet; the peak intensity of the radio core at this wavelength is 6.2 mJy.

#### *4.2.2 3C 55*

This source is a 69″ double previously imaged at radio wavelengths by Jenkins *et al.* (1977), Schilizzi *et al.* (1982), Strom & Conway (1985), and Leahy *et al.* (1989). Laing *et al.* (1983) gave an optical identification with a galaxy at $z=0.27$ but Spinrad (private communication, reported in Hewitt & Burbidge 1991) has since reidentified the source with a galaxy at $z=0.7348$. The radio core peaks at $\alpha=01^h54^m19^s.055$ and $\delta=28°37'2''.84$, and is slightly resolved (suggesting some jet emission is present). Leahy *et al.* also report the detection of this radio core at 5, 8, and 15 GHz at a preliminary position (Leahy 1992) $0^s.004$ earlier than ours in right ascension and 0″.07 north of ours in declination; both of these offsets are well within the errors of the radio observations. Both radio positions disagree by about 2″ in $\delta$ with that quoted by Spinrad of $\alpha=01^h54^m19^s.03$ and $\delta=28°37'00''.6$ for the revised optical identification, which is marked by a cross in Fig. 3. This discrepancy in declination leaves the new optical identification in some doubt.

Figure 3(b) shows the detailed structure of the eastern lobe. Several resolved features (F1 through F6) occur along the lower boundary of the lobe (Fig. 1). Features F2 (16.6 mJy peak), F6 (13.2 mJy peak), and F8 (30 mJy peak) have the highest surface brightnesses and are resolved (Table 6). However, F8 is the brightest feature in the eastern lobe, is $>4$ times brighter than the surrounding diffuse emission, and is $<1\%$ of the diameter of 3C 55, thus meeting our criteria for a hot spot. It is conceivable that features F1 through F6 might be part of a main jet in 3C 55 that is not detected within 22″ (120 kpc) of the core. This would be an exceptionally long "gap" for a jet in a radio galaxy, however, and more sensitive observations are needed to test whether this collection of features is indeed part of a jet, and not merely secondary structure in the lobe. The individual features are disparate in their alignment and polarization properties [see Fig. 3(b)], casting further doubt on their collective status as a jet.

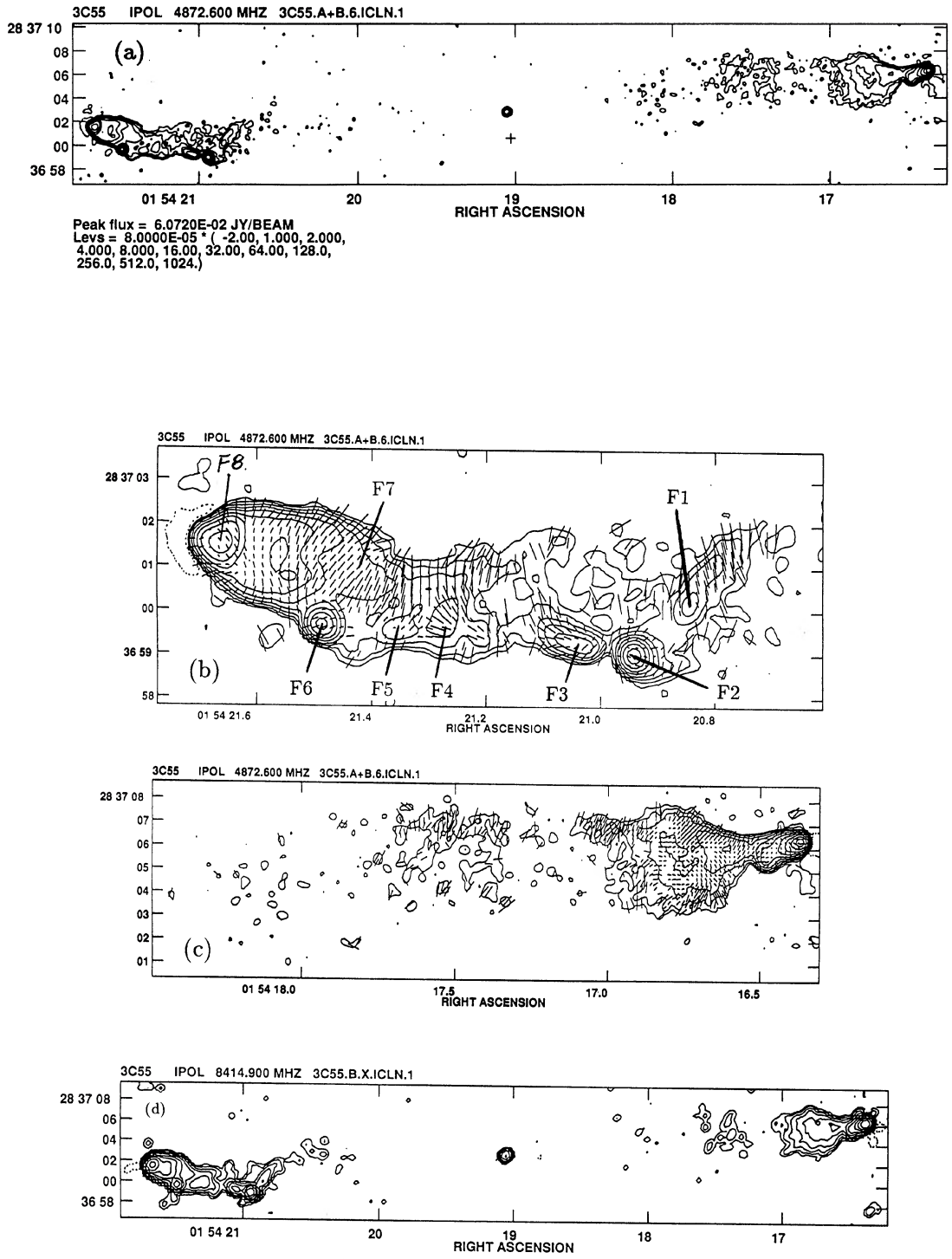


FIG. 3. (a) 6 cm total intensity map of 3C 55 at 0".35 from the combined A and B configuration data. (b) Contour map of the total intensity at 5 GHz of the eastern lobe of 3C 55 with polarization $E$ vectors overlaid. The contours levels are similar to those of (a). The vector scale is such that a vector length of 1 arcsec corresponds to $p=1.5$. (c) Same as (b), but for the western lobe of 3C 55. (d) Contour map of the total intensity of 3C 55 at 3.6 cm at 0".7 resolution from the B configuration. The contour levels are drawn at $-2$, 1, 2, 4, 8, 16,..., 128, 256, and 512 times 50 $\mu$Jy per CLEAN beam area. The peak flux density is $5.5\times10^{-2}$ Jy/beam. (e) 3.6 cm contour map of the total intensity of the eastern lobe of 3C 55 at 0".7 with polarization $E$ vectors overlaid. The contour levels are similar to those of (d). The vector scale is such that a vector length of 1 arcsec corresponds to $p=1.0$. (f) Same as (e), but for the western lobe of 3C 55. (g) Contour map of the total intensity of 3C 55 at 20 cm at 4".2 resolution with polarization $E$ vectors overlaid. The contour levels are drawn at $-2$, 1, 2, 4, 8, 16,..., 128, and 256 times 1.9 mJy per CLEAN beam area. The peak flux density is $7.4\times10^{-1}$ Jy/beam. The vector scale is such that a vector length of 1 arcsec corresponds to $p=0.1$.

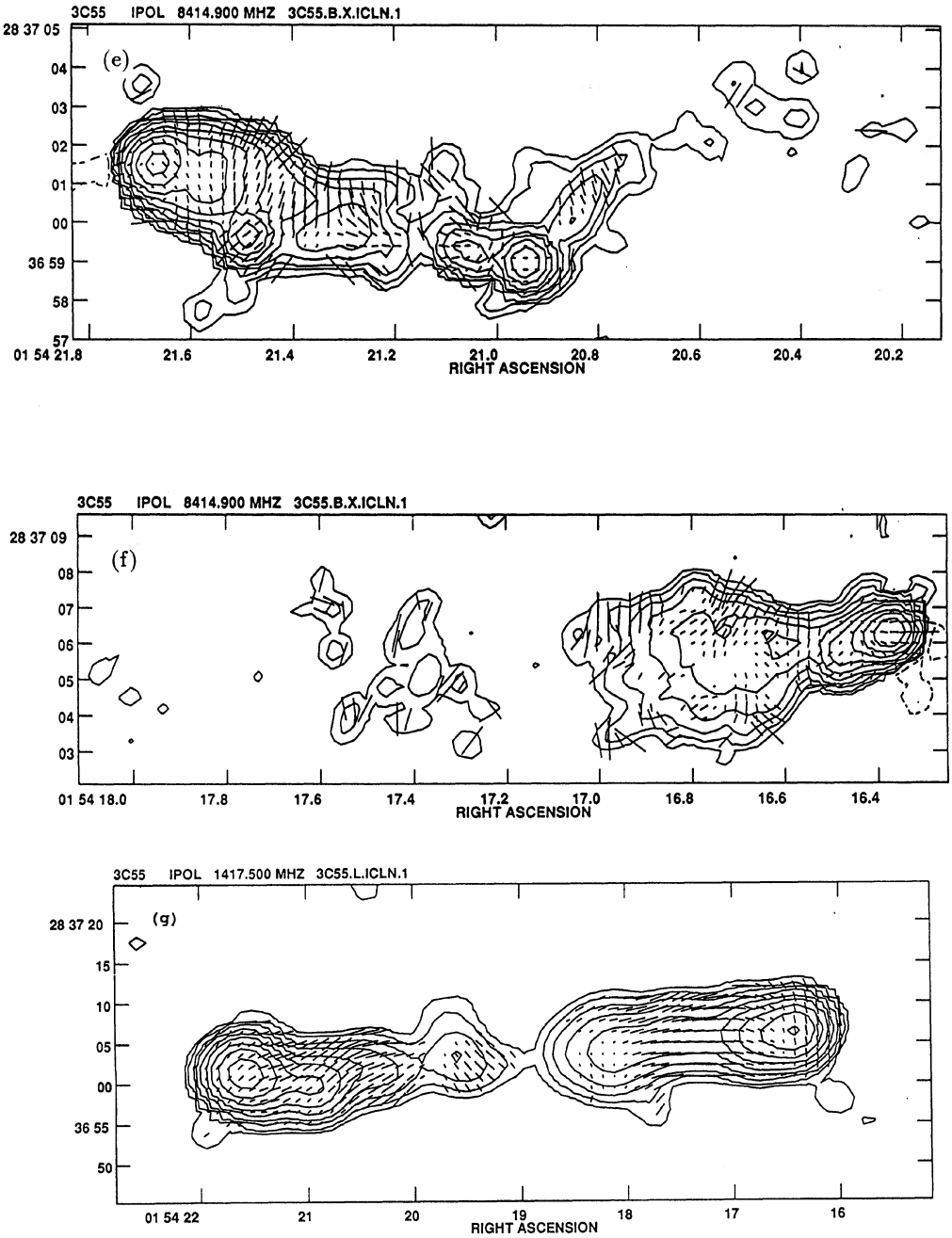


FIG. 3. (continued)

The western lobe, shown in detail in Fig. 3(c), has a striking "horn"-like structure. The opening angle of the "horn" is about 30° and appears to increase toward the core following an initially well-collimated structure near the western extremity of the lobe. Figure 3(c) also suggests that the western hot spot is connected to the horn structure by a narrow bridge. This structure resembles that seen in the numerical model of a restarting jet by Clarke & Burns (1991). Table 6 reports the hot spot sizes of each lobe, the core/lobe-feature distances, and the lobe flux densities at 5 GHz.

At 3.6 cm, the candidate jet of 3C 55 and the radio core are also detected [Fig. 3(d)] at a resolution of about 0".7. The peak intensity of the core is 3.4 mJy. Figures 3(e) and 3(f) reveal the detailed structures of the eastern and the western lobes at 3.6 cm with polarization $E$ vectors overlaid. Figure 3(g) shows a 20 cm contour map of the total intensity at 4".2 resolution with polarization $E$ vectors overlaid.

#### *4.2.3 3C 265*

Earlier resolved radio images of 3C 265 (Jenkins *et al.* 1977) revealed two lobes with an angular separation of

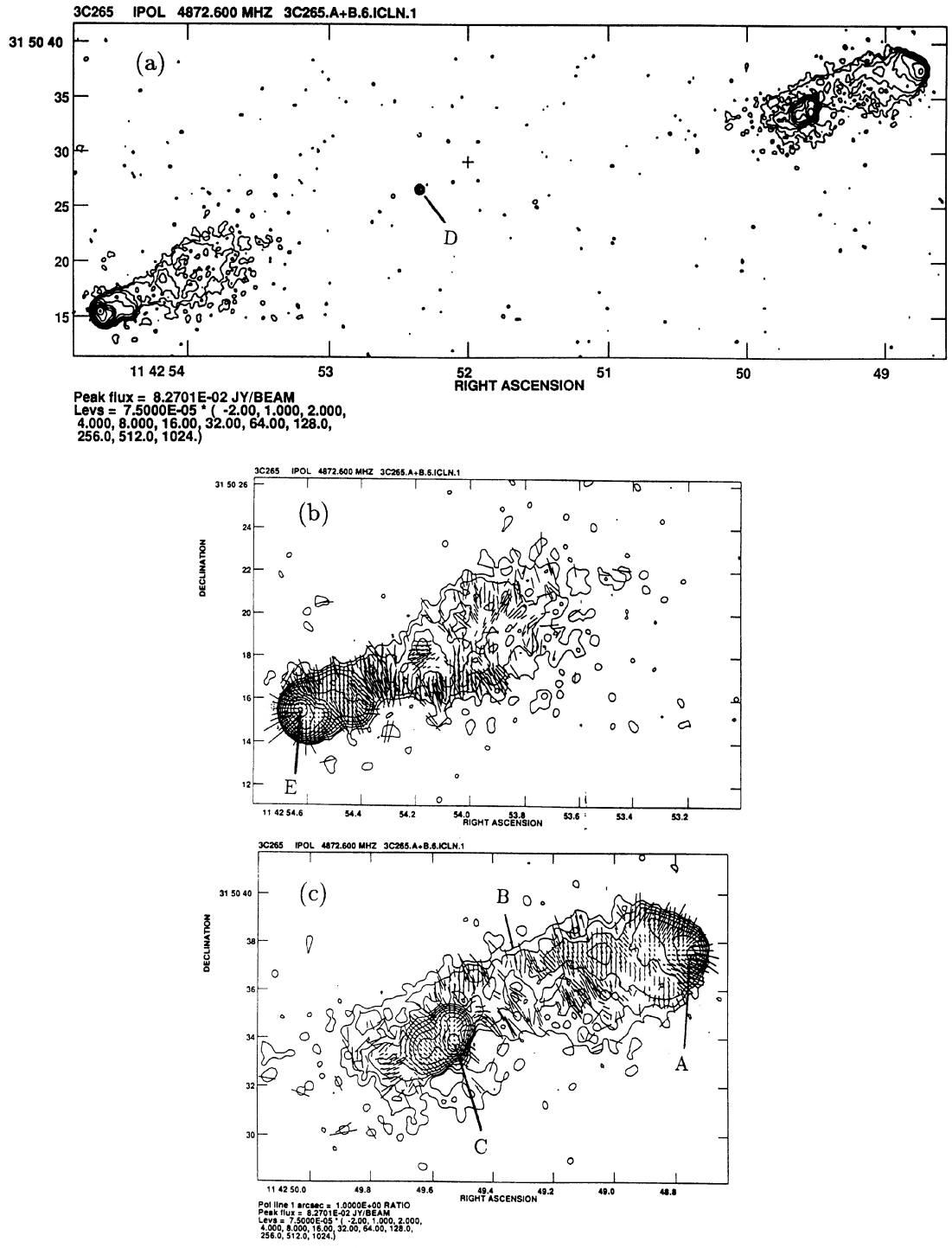


FIG. 4. (a) 6 cm contour map of the total intensity of 3C 265 at 0".35 resolution from the combined A and B configuration data. (b) 6 cm contour map of the total intensity of the SE lobe of 3C 265 with polarization $E$ vectors overlaid. (c) Same as (b), but for the NW lobe of 3C 265. (d) Contour map of the total intensity of 3C 265 at 3.6 cm at 0".7 resolution. The contour levels are drawn at $-2$, 1, 2, 4, 8, 16,..., 128, 256, and 512 times 50 $\mu$Jy per CLEAN beam area. The peak flux density is $6.7\times10^{-2}$ Jy/beam. (e) Contour map of the total intensity of the SE lobe of 3C 265 at 3.6 cm with polarization $E$ vectors overlaid. The contour levels are similar to those of (d). The vector scale is such that a vector of 1 arcsec corresponds to $p=1$. (f) Same as (e), but for the NW lobe of 3C 265. (g) 20 cm contour map of the total intensity of 3C 265 at 20 cm at 4".37 resolution with polarization $E$ vectors overlaid. The contour levels are drawn at $-2$, 1, 2, 4, 8, 16,..., 128, and 256 times 0.75 mJy per CLEAN beam area. The peak flux density is 1.15 Jy/beam. The vector scale is such that a vector of 1 arcsec corresponds to $p=0.1$.

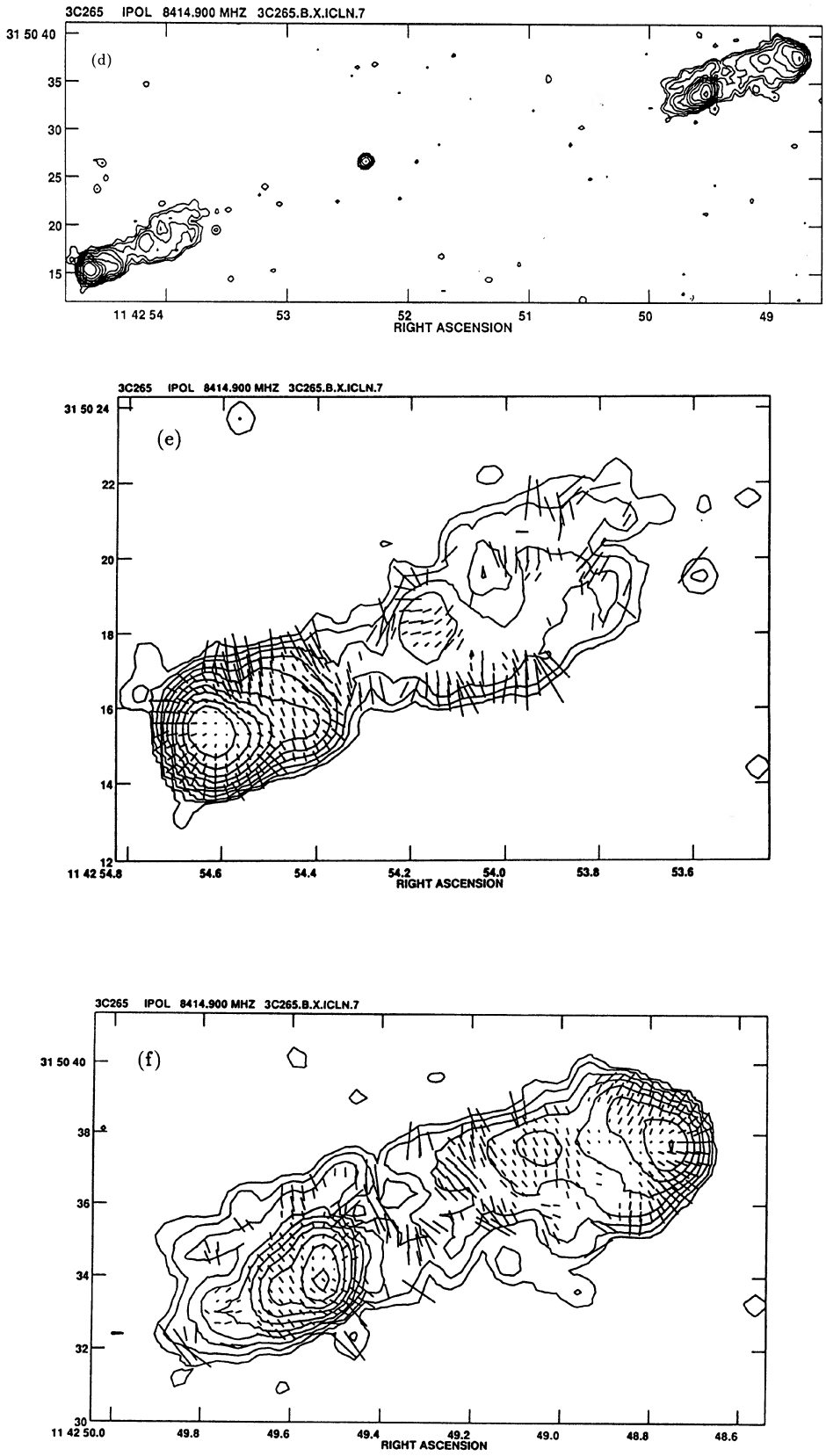


FIG. 4. (continued)

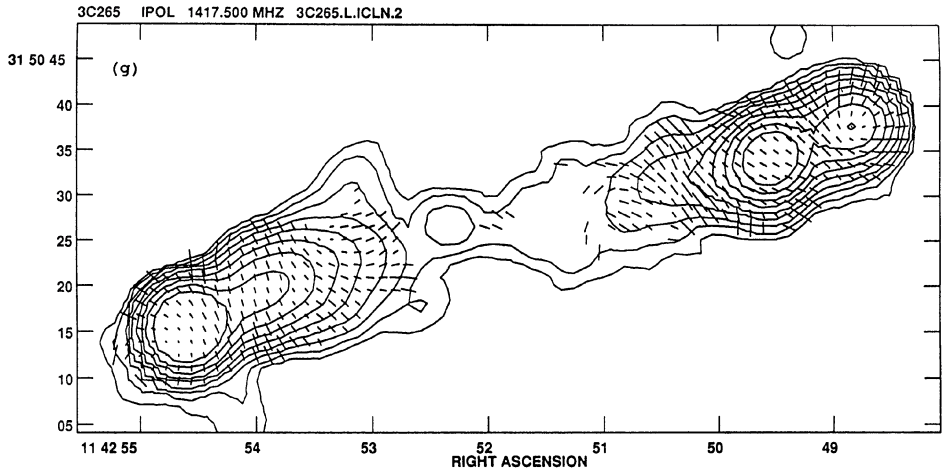


FIG. 4. (continued)

78″, multiple compact features in the western lobe, but no central small-diameter core. Figure 1 shows a greyscale display, and Fig. 4(a) shows a total intensity contour map at 5 GHz at 0.″4 resolution. The source has asymmetrically placed lobes, which broaden toward its center.

The 2.6 mJy core (*D*) is a new detection. Its peak is at $\alpha = 11^h42^m52^s.353$ and $\delta = 31°50'26''.61$. This is about 2.″5 from the optical identification proposed by Spinrad *et al.* (1985) at $\alpha = 11^h42^m52^s.39$ ($\pm 0^s.08$) and $\delta = 31°50'29''.1$ ($\pm 1''.0$), shown by the cross in Fig. 4(a). This positional discrepancy leaves the validity of the optical identification in doubt.

Figures 4(b) and 4(c) show the SE and NW lobes of 3C 265, respectively. The NW lobe contains two bright regions (*A* and *C*), connected by a faint elongated bridge (*B*). Feature *C* (34.3 mJy peak) is considerably brighter than *A* (5.4 mJy peak), is slightly more than four times brighter than the surrounding lobe emission, and is $< 1\%$ of the diameter of 3C 265. Thus, *C* meets our conditions for being labeled the hot spot in the western lobe. It is unclear if the bridge between *A* and *C* constitutes a candidate jet in 3C 265.

There is no sign of a counterjet on the other side of the source. The SE lobe has a bright hot spot (*E*) at its end. The axis through the SE hot spot and features *C* and *A* does not cross the radio core. There is no sign of a counterjet on the SE side of the source.

Figures 4(b) and 4(c) also show the polarization *E* vectors overlaid for the SE and NW lobes, respectively. Features *A*, *C*, and *E* are relatively highly (25%) polarized. The edges of the two lobes are also highly polarized (35%–45%), with the *E* vectors perpendicular to the local ridge lines.

Figure 4(d) shows a total intensity contour map at 3.6 cm at 0.″7 resolution from the B configuration. As in the 6 cm high resolution maps, the radio core is also detected. Its peak intensity is 1.6 mJy. Figures 4(e) and 4(f) show the SE and the NW lobes of 3C 265 at 3.6 cm with polarization *E* vectors overlaid. The polarized radio emission appears to be evenly distributed in both lobes. The 20 cm total intensity map at 4.″4 resolution with polarization vectors is shown in Fig. 4(g).

#### *4.2.4 3C 324*

An early image of 3C 324 (Jenkins *et al.* 1977) showed an asymmetric double with a 10″ lobe spacing. 3C 324 is the smallest source in our sample, and its internal structure is only marginally resolved by our data. Figure 1 shows a greyscale image and Fig. 5(a) shows a total intensitycontour map at 5 GHz at 0.″34 resolution.

The optical identification proposed by Gunn *et al.* (1981) at $\alpha = 15^h47^m37^s.1$ ($\pm 0^s.08$) and $\delta = 21°34'40''.1$ ($\pm 1''.0$) is shown by the cross in Fig. 5(a). This object is apparently one of the most luminous known galaxies. It is now thought (Le Fèvre *et al.* 1987; Hammer & Le Fèvre 1990) to be a gravitational mirage produced by the superposition of a foreground, possibly spiral, galaxy at $z = 0.845$ on a background narrow-line galaxy at $z = 1.206$. There is a faint, relatively compact radio feature (*C*) near the SW lobe of 3C 324. The peak intensity (0.38 mJy) of this feature is located at $\alpha = 15^h47^m37^s.05$ and $\delta = 21°34'40''.8$. This feature is about 1″ from the proposed optical identification of Gunn *et al.* It is unclear, however, if *C* is the radio core of the source, part of a jet or a counterjet, or a compact feature in the radio lobe. A 2-D elliptical Gaussian fit indicates that this feature is well resolved with a deconvolved FWHM of $0''.38 \times 0''.30$ (2.2 kpc × 1.7 kpc), casting doubt on its being the radio core.

Figure 5(a) shows hot spots (*A* and *E*) in the two lobes. Both *A* and *E* have deconvolved widths which are slightly less than 5% of the source major axis, and are greater than four times brighter than the surrounding lobe emission. The SW lobe has a broad extension (*B*) toward the center of the source. The NE lobe, besides its hot spot, has a narrow feature (*D*); this narrow feature is a candidate for a jet or a bright lobe filament, but we cannot determine which at this resolution.

Table 6 reports the sizes of hot spots *A* and *C*, and the flux densities of the NE and SW lobes at 5 GHz. The total

integrated flux density of 3C 324 at 5 GHz is 0.64 Jy. Besides their differences in flux density, the two lobes are also located asymmetrically with respect to the feature (*C*).

Figures 5(b)–5(d) show polarization maps of 3C 324 at 6, 3.6, and 20 cm at a resolution of 0.″4, 0.″7, and 4.″1, respectively. In Sec. 5, we show that the SW lobe is more strongly depolarized than the NE lobe—a common asymmetry in classical doubles (Garrington *et al.* 1988; Laing 1988).

*4.2.5 3C 356*

A previous radio image of 3C 356 by Pedelty *et al.* (1989) showed two radio lobes with an angular separation of 72″, but no core or jet. Figure 1 shows a greyscale image and Fig. 6(a) shows a total intensity contour map of 3C 356 at 5 GHz at 0.″38 resolution.

Our observations show two compact radio features, (*D*) and (*E*), in the inner part of the source. The peak of the brighter feature, (*D*), is at $\alpha = 17^h23^m06^s.955$ and $\delta = 51°00'14''.15$, in good agreement with that of the optical

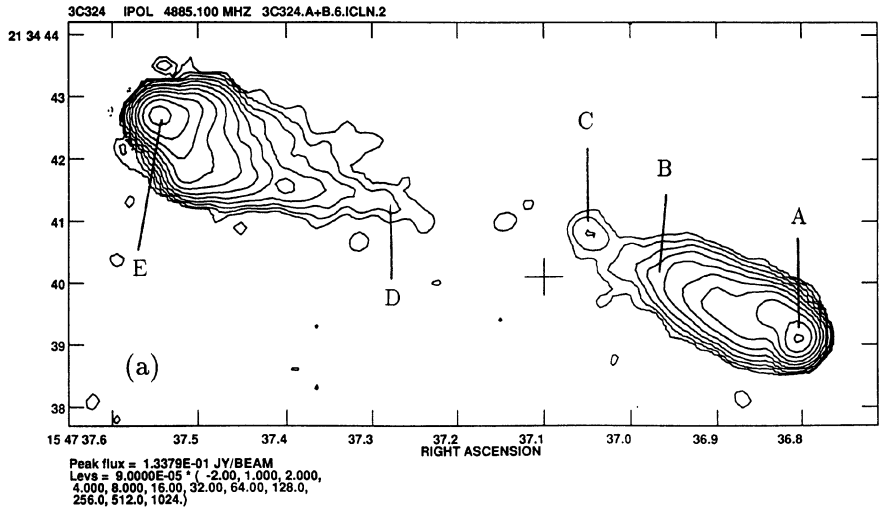


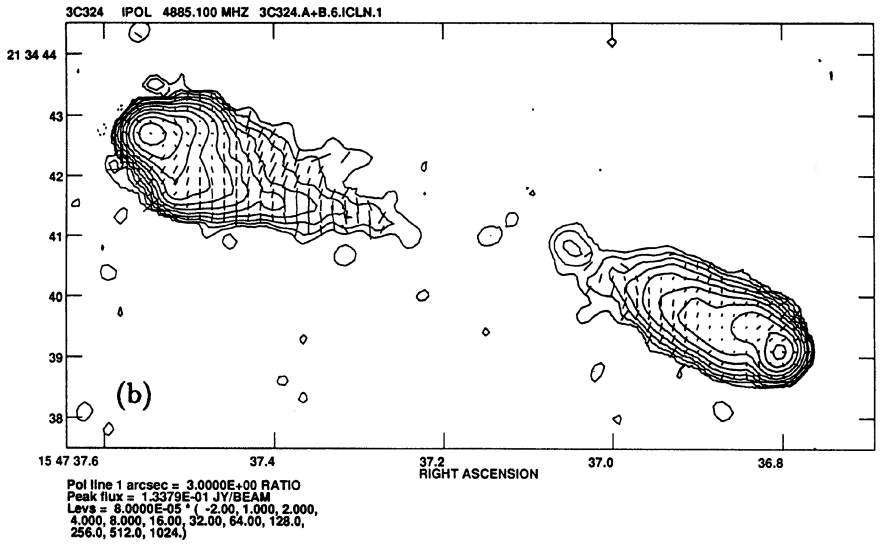


FIG. 5. (a) 6 cm contour map of the total intensity of 3C 324 at 0.″34 resolution from the combined A and B configuration data. (b) 6 cm contour map of the total intensity of 3C 324 at 0.″34 resolution with polarization *E* vectors overlaid. (c) 3.6 cm contour map of the total intensity of 3C 324 at 0.″7 resolution with polarization *E* vectors overlaid. The contours levels are drawn at $-2$, 1, 2, 4, 8, 16,..., 128, and 256 times 100 $\mu$Jy per CLEAN beam area. The peak flux density is $1.2\times10^{-1}$ Jy/beam. The vector scale is such that a vector of 1 arcsec corresponds to $p=1.3$. (d) 20 cm contour map of the total intensity of 3C 324 at 4.″1 resolution with polarization *E* vectors overlaid. The contour levels are drawn at $-2$, 1, 2, 4, 8, 16,..., 128, and 256 times 2.1 mJy per CLEAN beam area. The peak flux density is 1.48 Jy/beam. The vector scale is such that a vector of 1 arcsec corresponds to $p=0.12$.

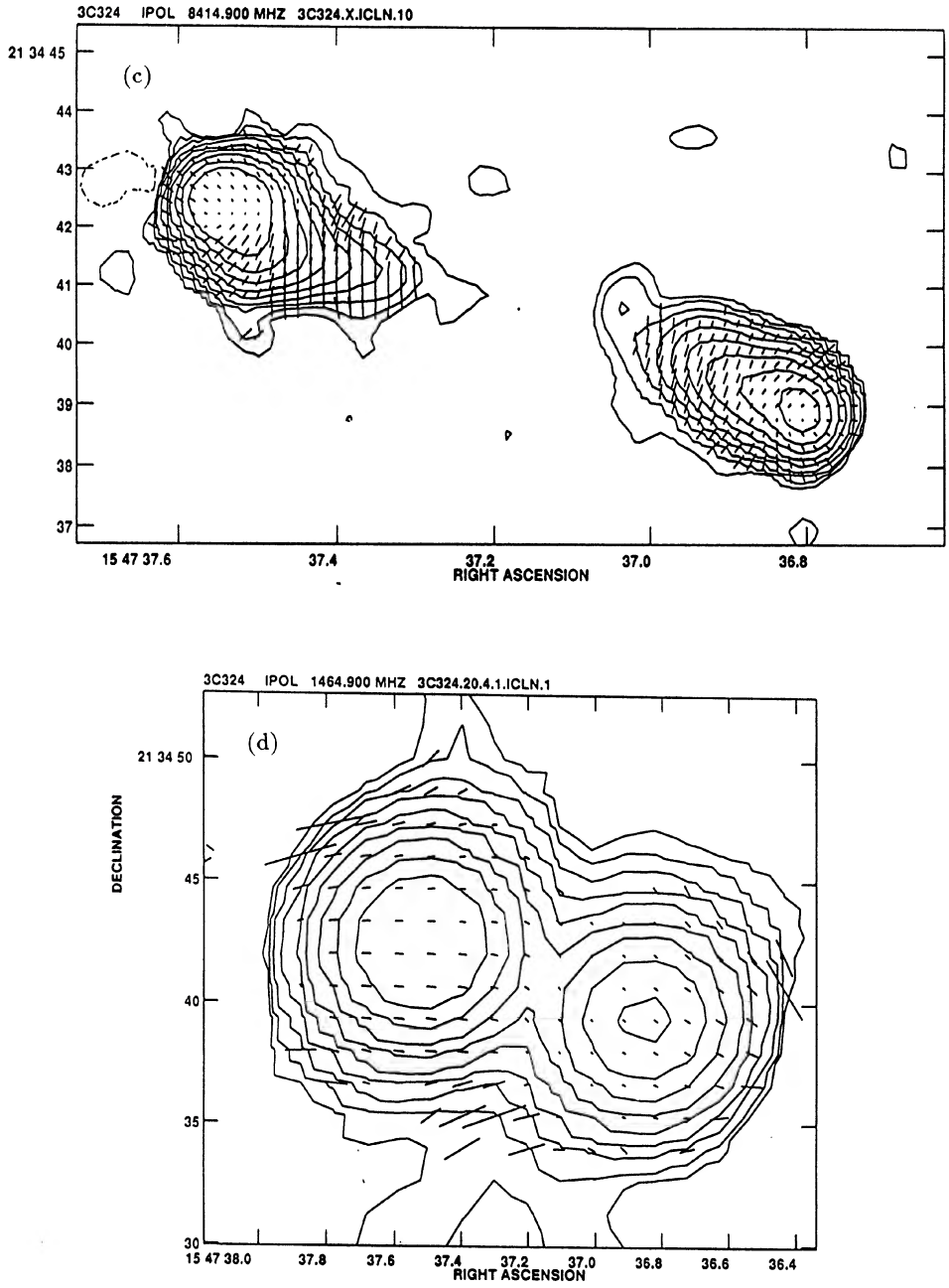


FIG. 5. (continued)

identification suggested by Spinrad *et al.* (1985), which is at $\alpha = 17^h23^m06^s.96$ and $\delta = 51°00'14''.1$. This peak also appears to coincide with the compact peak of the resolved 2.2 $\mu$m feature (b) detected by Eales & Rawlings (1990) and by Eisenhardt & Choksi (1990). This coincidence does not, however, uniquely establish the optical identification of the extended radio structure; there is a similarly good positional agreement between another galaxy noted by Riley *et al.* (1980) at $\alpha = 17^h23^m06^s.66$ ($\pm 0^s.20$) and $\delta = 51°00'18''.2$ ($\pm 2''.0$), the compact 2.2 $\mu$m feature (a) in both Eales & Rawlings (1990) and Eisenhardt & Choksi (1990), and the fainter radio peak ($E$) at $\alpha = 17^h23^m06^s.663$ and $\delta = 51°00'18''.09$. Rigler *et al.* (1992) suggest that ($a/E$) is the parent of the radio structure because this galaxy has a higher ionization spectrum. They also suggest that ($b/D$), which exhibits an extended optical emission line system, is a companion galaxy that has wandered into the path of an unseen radio jet emanating from ($a/E$).

Gaussian fits to our 6 cm data show that both ($D$) and ($E$) are unresolved (Table 5). Our 3.6 cm data detect both ($D$) and ($E$) at a resolution of $0''.84$ [Fig. 6(d)] with peak

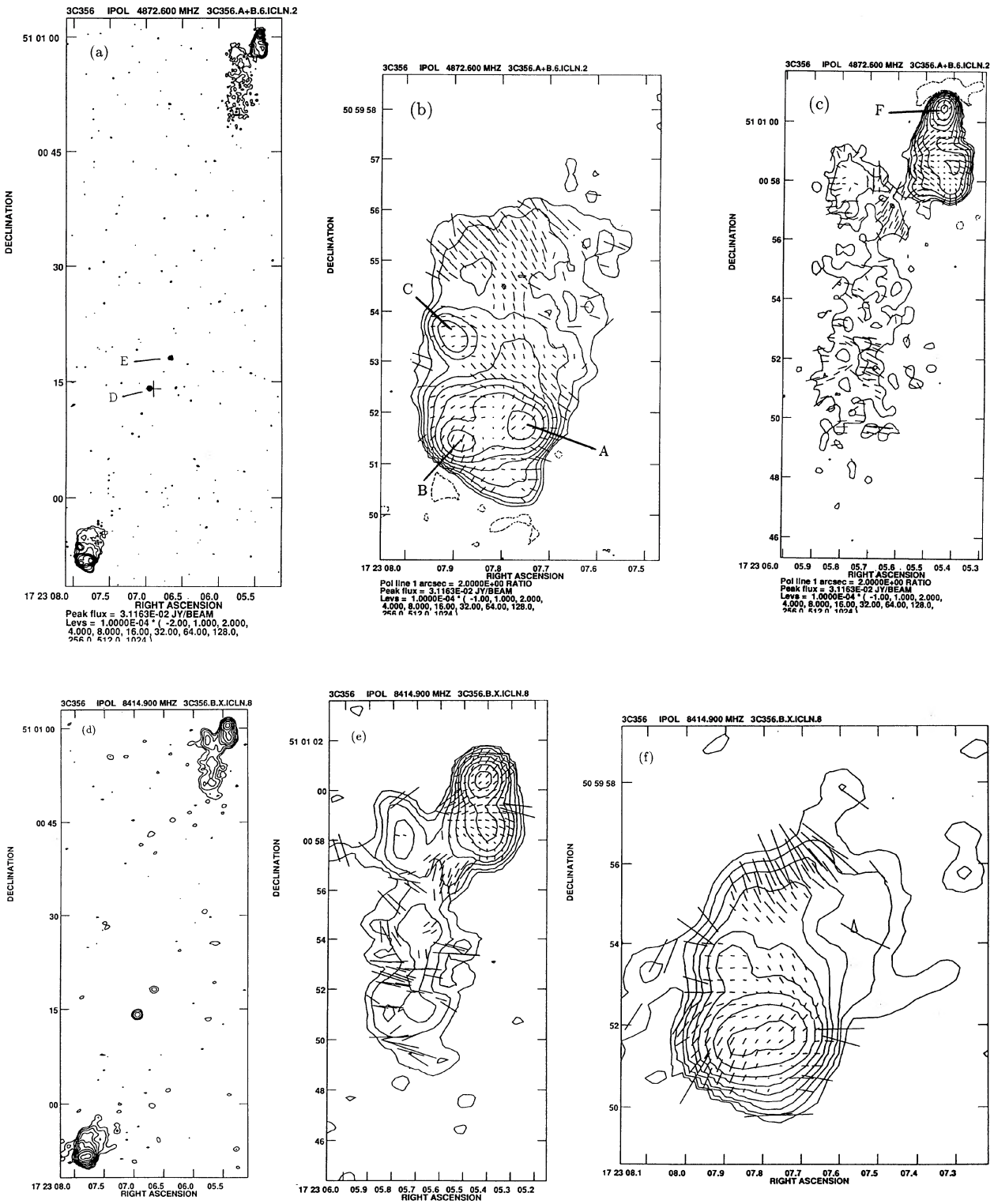


FIG. 6. (a) 6 cm contour map of the total intensity of 3C 356 at 0″38 resolution from the combined A and B configuration data. (b) 6 cm contour map of the total intensity of the southern lobe of 3C 356 with polarization $E$ vectors overlaid. (c) Same as (b), but for the northern lobe of 3C 356. (d) 3.6 cm contour map of the total intensity of 3C 356 at 0″84 resolution. The contour levels are drawn at $-2$, 1, 2, 4, 8, 16,..., 256, and 512 times 70 $\mu$Jy per CLEAN beam area. The peak flux density is $2.45\times10^{-2}$ Jy/beam. (e) 3.6 cm contour map of the total intensity of the northern lobe of 3C 356 with polarization $E$ vectors overlaid. The contour levels are similar to those of (d). The vector scale is such that a vector length of 1 arcsec corresponds to $p=0.67$. (f) Same as (e), but for the southern lobe of 3C 356. (g) 20 cm contour map of the total intensity of 3C 356 at 3″9 resolution with polarization $E$ vectors overlaid. The contour levels are drawn at $-2$, 1, 2, 4, 8, 16,..., 128, and 256 times 0.8 mJy per CLEAN beam area. The peak flux density is $6.23\times10^{-1}$ Jy/beam. The vector scale is such that a vector length of 1 arcsec corresponds to $p=0.12$.

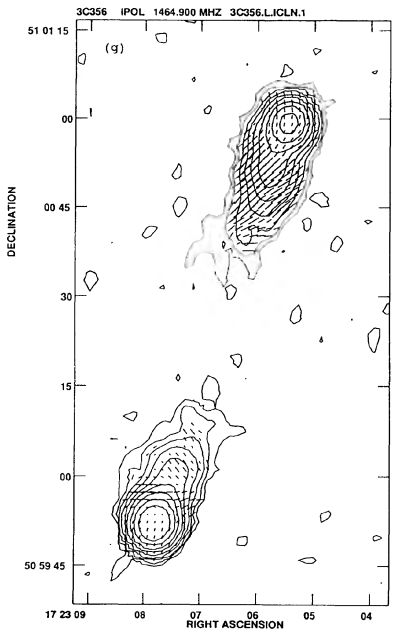


FIG. 6. (continued)

flux densities of 1.05 and 0.25 mJy, respectively. Thus, the 6 to 3.6 cm spectral indices (defined by $S_\nu \propto \nu^{-\alpha}$) of (*D*) and (*E*) are 0.1 and 1.1, respectively. (*D*), therefore, has the more typical spectral index for the compact core of an extended radio galaxy, whereas (*E*) has a spectral index more typical of a steep-spectrum, compact source.

We conclude that the available data on the two compact radio features near the center of 3C 356 do not resolve the identification ambiguity uniquely. Instead, both (*a*/*D*) and (*b*/*E*) display several characteristics of active galactic nuclei and it cannot yet be determined which galaxy is responsible for the large-scale radio structure. This ambiguity may remain until more sensitive radio images detect a large-scale radio jet linking one of these two nuclei to the radio lobes.

Figures 6(b) and 6(c) show enlargements of the SE and NW lobes of 3C 356 at the same 0".38 resolution with polarization *E* vectors overlaid. The SE lobe [Fig. 6(b)] contains three compact structures (A, B, and C) of which (A) and (B) are of approximately equal brightness. The NW lobe [Fig. 6(c)] has a better defined hot spot (*F*) and a much larger trail of extended emission than the SE lobe. The results of fitting 2-D elliptical Gaussian models to features (A), (B), (C), and (F) are given in Table 6, along with the NW and SE lobe flux densities.

Figures 6(e) and 6(f) reveal the detailed structures of the northern and southern lobes of 3C 356 with polarization *E* vectors overlaid. Figure 6(g) shows a contour map of the total intensity at 20 cm at 3".9 resolution from the B configuration.

## 5. DEPOLARIZATION ANALYSIS

Because our three-frequency polarization data were taken only in the B configuration, images made from the untapered data have different resolutions, $\approx$0".7 at 3.6 cm, $\approx$1".1 at 6 cm, and $\approx$4".0 at 20 cm. The images made from these tapered data cannot be expected to measure small depolarization differences reliably, as they have differing sensitivities to large- and small-scale structures at the two frequencies. We have, therefore, tapered the $(u,v)$ data to obtain similar resolutions of 1".1 at 3.6 and 6 cm, and of 4" at 6 and 20 cm. The resulting tapered maps should be adequate to give a preliminary indication of any gross depolarization asymmetries across these sources.

TABLE 7. Mean depolarization ratios, DP, for the RG lobes.

| | $DP^6_{3.6}$ | | $DP^{20}_6$ | |
|---|---|---|---|---|
| 3C 22 | NW 0.9(0.2) | SE 1.0(0.3) | NW 1.1(0.4) | SE 0.3(0.1) |
| 3C 55 | SE 0.7(0.1) | NW 0.8(0.2) | SE 1.0(0.3) | NW 0.8(0.3) |
| 3C 265 | NW 1.2(0.2) | SE 1.0(0.2) | NW 0.9(0.3) | SE 1.0(0.4) |
| 3C 324 | SW 1.0(0.3) | NE 0.9(0.3) | SW 0.7(0.3) | NE 0.2(0.1) |
| 3C 356 | NW 1.0(0.1) | SE 0.9(0.1) | NW 0.6(0.1) | SE 0.5(0.2) |

Note to TABLE 7.

Errors are given in parentheses.

We define the depolarization ratio, DP, as the ratio of the fractional polarization of the longer wavelength ($\lambda_2$) to that of the shorter wavelength ($\lambda_1$)

$$\mathrm{DP}=\frac{p(\lambda_2)}{p(\lambda_1)}, \quad (1)$$

where $p$ is the fractional polarization at $\lambda_2$ and $\lambda_1$ for each component of the radio source. Table 7 reports the mean depolarization ratio of each side of the radio galaxy. This mean was computed over a region of about 5 beamwidths centered around the peak of each lobe. The mean DP was computed by summing over the $I$ and $P$ maps at each frequency which were first blanked below the $4\sigma$ contour level. This reduced the amount of blank-sky bias in the sums on the $p$ maps.

The compilation of Tabara & Inoue (1980) estimates half-depolarization wavelengths of 17 cm for 3C 356, 23 cm for 3C 324, >21 cm for 3C 22 and 3C 55, and >31 cm for 3C 265. Our depolarization data (Table 7) generally agree with Tabara and Inoue's results in that neither 3C 55 nor 3C 265 shows significant depolarization between 8.4 and 1.4 GHz, and the other three sources show depolarization only between 4.9 and 1.4 GHz.

Strom & Conway (1985) report asymmetric depolarization in 3C 55 and 3C 265 between 1.4 and 0.5 GHz at 20".3$\times$20".3 csc $\delta$ resolution. Their lower frequency data are the only evidence for depolarization in these sources. For 3C 324, there is an apparent discrepancy between our results and the earlier work of Conway *et al.* (1983) and of Pedelty *et al.* (1989). We find that the NE lobe is significantly more depolarized at 20 cm, whereas Conway *et al.* quote half-depolarization wavelengths of 15 and 22 cm for the SW and NE lobes, respectively. Pedelty *et al.* find the lobes to be equally depolarized on average, with the strongest depolarization being in the trailing portion of the western lobe. We conclude that the depolarization asymmetry of 3C 324 is poorly established at present.

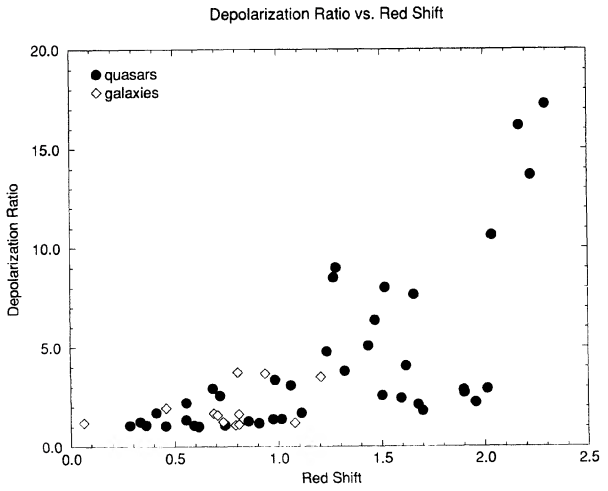


FIG. 7. Plot of the depolarization ratio for the two radio lobes vs redshift for a sample of quasars and radio galaxies. These data are from Garrington *et al.* (1991) and this paper.

For 3C 22, our data provide new evidence for a significant depolarization asymmetry between 6 and 20 cm—the side that depolarizes at the shorter wavelength being that with the fainter, or counter, jet. For 3C 356, we find significant depolarization in both lobes between 6 and 20 cm, symmetric to within our errors. This result conflicts with that of Pedelty *et al.* (1989) who found depolarization only in the south lobe between these wavelengths. We conclude that the depolarization asymmetry of 3C 356 is also poorly established.

Figure 7 plots the lobe depolarization asymmetry ratios versus redshifts for the sample of radio galaxies and quasars that results from combining the Garrington *et al.* (1991) sample with our new measurements. The upper envelope of this plot clearly reaches to much higher depolarization ratios for the QSRs at the higher redshifts. The origin of this effect is unclear, though it may be related to higher circumgalactic densities and magnetic fields around the objects at higher redshifts. For our present purpose, however, Fig. 7 emphasizes that we must compare the depolarization asymmetries of radio galaxies and QSRs at similar redshifts to avoid confusion with the apparent $z$ dependence. If we consider only the data for $z < 1.2$, there is no evidence for any difference in the depolarization ratios between the RGs and QSRs, but the numbers of objects in both samples are small.

Recently, Conway *et al.* (1992) examined the unsigned depolarization ratios for 13 QSRs and 23 RGs at redshifts in the range $0.3 < z < 1$. They found that the histogram of depolarization ratios had more values close to 1.0 for the radio galaxies than for the quasars, suggesting that the depolarization asymmetry is weaker for the galaxies. As our own, albeit smaller, sample does not confirm this effect, we believe that better statistics may be needed before a definitive conclusion is reached on this issue.

## 6. JET AND OPTICAL EMISSION LINE ASYMMETRIES

For some of the RGs listed in Table 1, CCD broad and narrow band [O II] optical images were available to us from McCarthy (1988). The location of any extended optical emission line regions relative to the radio jets and lobes may offer clues to the origin of the separation asymmetry of the lobes and the brightness asymmetries of the jets. McCarthy *et al.* (1987, 1991) report that the radio asymmetries (primarily the core-lobe separation asymmetry on opposite sides of the source) of powerful radio sources are strongly correlated with the asymmetry of the emission line regions, in that any asymmetrical line emission favors the side of the nucleus that has the closer radio lobe. They inferred that the core-lobe distance asymmetries have an environmental origin.

We re-examined the radio–optical relationships by overlaying our new radio images onto the optical emission line images from McCarthy (1988). We aligned the peak of the optical emission with the radio galaxy position in each case. The overlays are shown in Fig. 8. For 3C 22, McCarthy noted that the optical emission line region is unresolved (the extension to the north is an artifact of the data processing), so no conclusion can be drawn regarding the jet asymmetry. Above, we noted that the counterjet side is more depolarized than the jet side. For 3C 55, no optical image was available to us. For 3C 265, the brighter [O II] emission is on the SE side of the nucleus, but there is evidently also an extended [O II] emission region towards the NW. Thus, the brighter emission line region is on the side of the shorter radio lobe, but it is notable that there is significant line emission on both sides, no significant depolarization at 20 cm on either, and greater depolarization at 49 cm on the side of the longer radio lobe. For 3C 324, the emission line gas is extended along the radio source axis but there is no clear indication of an [O II] emission asymmetry or of a depolarization asymmetry. The symmetries of the optical data for this source may also be complicated by gravitational lensing (see Sec. *4.2.4*). For 3C 356, the relation between the [O II] line-emitting gas and the radio source is complicated by the uncertainty in the optical identification (Sec. *4.2.5*). We note, however, that the SE lobe must be closer whether either feature *D* or feature *E* marks the parent object of the extended radio structure. Our data show that the SE (closer) lobe is not strongly depolarized at 20 cm, and the NW (further) lobe is the more strongly polarized at longer wavelengths (Strom & Conway 1985).

We conclude that there is no clear correlation between the depolarization asymmetries of these sources and either their emission line asymmetries or their lobe-length asymmetries.

## 7. DISCUSSION

The high resolution and high dynamic range of our 6 cm images have allowed us to define many new features associated with these five FRII radio galaxies.

First, we have detected the radio cores of at least four

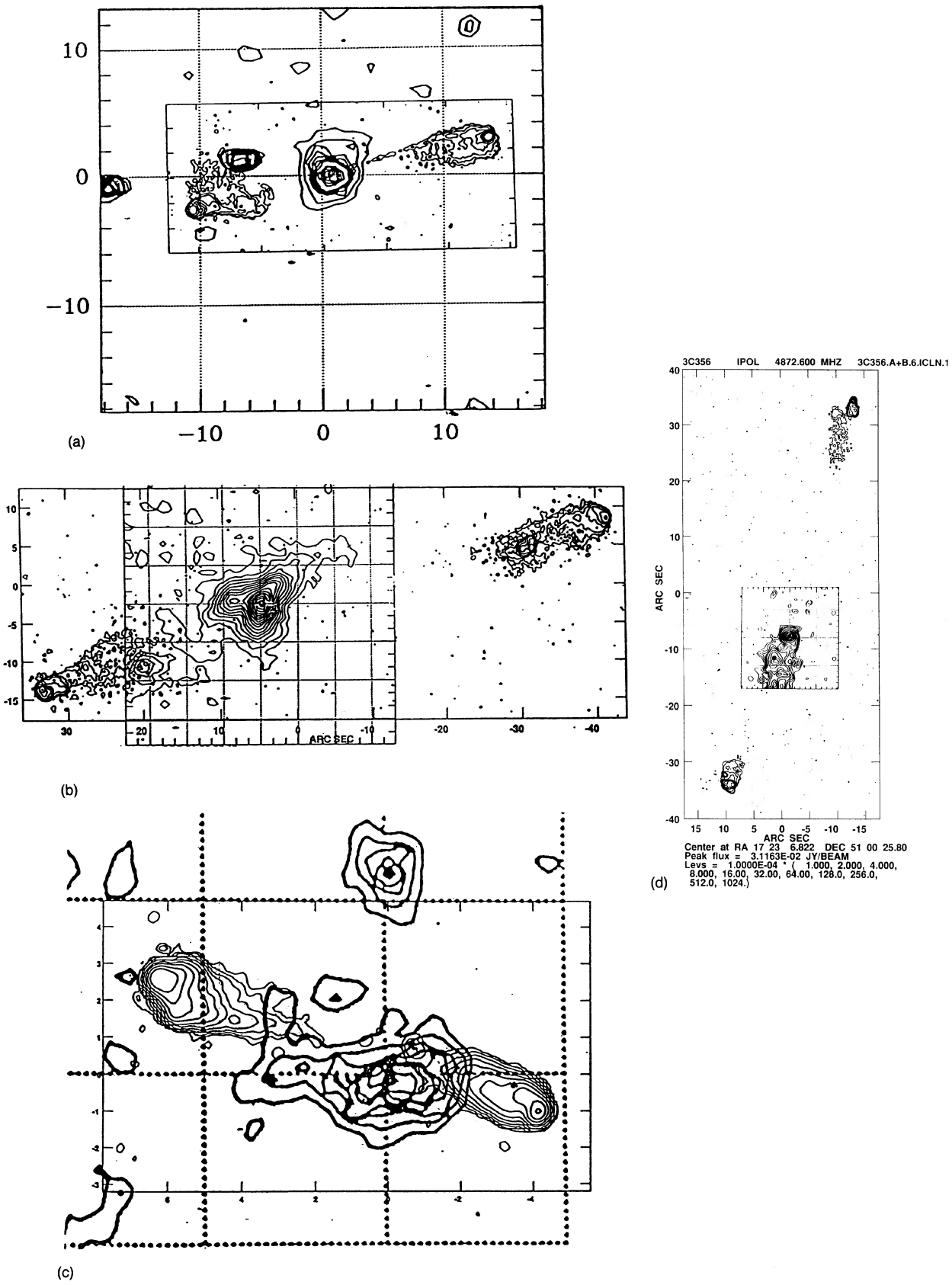


FIG. 8. Overlays of the narrow band [O II] optical images (bold contours) from McCarthy (1988) onto VLA 6 cm images of 3CR radio galaxies. (a) is 3C 22, (b) is 3C 265, (c) is 3C 324, and (d) is 3C 356.

RGs—three for the first time. These detections confirm the optical identification of 3C 22, but cast some doubt on the identifications of 3C 55, 3C 265, and 3C 356. For 3C 55, the offset is about 2″ in $\delta$ between the radio and optical positions. For 3C 265, the offset of the radio core position and the optical identification is 2″.5. In both cases, more accurate optical positions are now needed to confirm the proposed identifications. For 3C 356, it is unclear if feature (*D*) or (*E*) is the radio core—both are associated with galaxies. However, *D* has a flat radio spectrum more typical of compact radio cores. Only a deeper radio image that is able to trace a radio jet into one or the other can resolve the ambiguity for 3C 356.

Second, a definite radio jet has been detected only in 3C 22. Candidate jets or jet components are present in 3C 55, 3C 265, and 3C 324, but in all three cases there is a strong possibility of confusion with lobe edge-brightening or filaments. None of these putative jets meets our quantitative criteria for a jet. The low (1 in 5) rate of unambiguous jet detections in this sample stands in strong contrast to the observations of a comparison group of extended 3CR QSRs by Bridle *et al.* (1993), in which 13 of 13 objects have unambiguous jets according to the same quantitative criteria. We consider this result to be the most significant of this study so far. The much lower incidence of detectable jets in this sample of radio galaxies is broadly consistent with the RG/QSR unification scheme proposed by Barthel (1989) and with the trends of jet-to-lobe prominence in a larger sample of RGs and QSRs at these powers derived by Bridle (1992).

Section 5 showed that there is little depolarization in these five radio galaxies as the wavelength increases from 3.6 to 6 cm, but three (3C 22, 3C 324, and 3C 356) show significant depolarization between 6 and 20 cm. 3C 22, the only source in this group in which we have detected an unambiguous radio jet, has a strong depolarization asymmetry with the jetted lobe being the less depolarized at 20 cm. In both 3C 324 and 3C 356, the sign of the depolarization asymmetry is unclear, while both 3C 55 and 3C 265 exhibit asymmetric depolarization at longer wavelengths. Combining our data with those of Garrington *et al.* (1991), we found no evidence for differences in the lobe depolarization asymmetry between RGs and QSRs *at similar redshifts*, but the sample is small.

Section 6 used our improved images to confirm the result of McCarthy *et al.* (1987, 1991) that, in sources in which the extended optical emission line system is markedly asymmetric, there is more emission line gas on the shorter side of the radio source. This suggests that the separation asymmetry of the lobes may be related to an asymmetry in the ambient gas density that slows the development of one lobe relative to the other. There is no evidence from our data, however, for any further correlation between the emission line asymmetries and jet sidedness or depolarization asymmetries.

Later papers will present the VLA data on the other sources in Table 1, and will compare the core, jet, and lobe properties of this radio galaxy sample with those of the quasars from Bridle *et al.* (1993).

This paper was derived from part of the Ph.D. dissertation of I. Fernini presented to the University of New Mexico. We thank the NRAO AIPS group for the software used in the data reduction and analysis, and Drs. J. P. Leahy and P. J. McCarthy for providing us with their VLA data. We also thank Linda Rasmussen of the NMSU Visualization Center for her help in preparing Fig. 1, and Chris Loken for his comments on the text and his help with Fig. 1. This work was supported by NSF Grant No. AST-9012353 to J.O.B.

## REFERENCES

Baars, J. W. M., Genzel, R., Pauliny-Toth, I. I. K., & Witzel, A. 1977, A&AS, 61, 9
Barthel, P. D. 1989, ApJ, 336, 606
Blandford, R. D., & Königl, A. 1979, ApJ, 232, 34
Bridle, A. H., & Perley, R. A. 1984, ARA&A, 22, 319
Bridle, A. H. 1990, in Parsec-Scale Radio Jets, edited by J. A. Zensus and T. J. Pearson (Cambridge University Press, New York), p. 186
Bridle, A. H. 1992, in Testing the AGN Paradigm, AIP Conference Proceedings No. 254, edited by S. S. Holt, S. G. Neff, and C. M. Urry, p. 386
Bridle, A. H., Hough, D. H., Lonsdale, C. J., Burns, J. O., & Laing, R. A. 1993, in preparation
Clarke, D. A., & Burns, J. O. 1991, ApJ, 369, 308
Conway, R. G., Birch, P., Davis, R. J., Jones, L. R., Kerr, A. J., & Stannard, D. 1983, MNRAS, 202, 813
Conway, R. G., Garrington, S. T., & Holmes, G. 1992, in Extragalactic Radio Sources—From Beams to Jets, Proceedings of the 7th IAP Meeting, edited by J. Roland, H. Sol, and G. Pelletier (Cambridge University Press, Cambridge), p. 279
Cotton, W. D. 1989, in Synthesis Imaging in Radio Astronomy, edited by R. A. Perley, F. R. Schwab, and A. H. Bridle (ASP, San Francisco), p. 233
Eales, S. A., & Rawlings, S. 1990, MNRAS, 243, 1P
Eisenhardt, P., & Choksi, A. 1990, ApJ, 351, L9
Fanaroff, B. L., & Riley, J. M. 1974, MNRAS, 167, 31P
Fernini, I., Leahy, J. P., Burns, J. O., & Basart, J. P. 1991, ApJ, 381, 63
Fomalont, E. B., & Perley, R. A. 1989, in Synthesis Imaging in Radio Astronomy, NRAO Workshop No. 21, edited by R. A. Perley, F. R. Schwab, and A. H. Bridle (ASP, San Francisco), p. 113
Garrington, S. T., Leahy, J. P., Conway, R. G., & Laing, R. A. 1988, Nature, 331, 147
Garrington, S. T., Conway, R. G., & Leahy, J. P. 1991, MNRAS, 250, 171
Gunn, J. E., Hoessel, J. G., Westphal, J. A., Perryman, M. A. C., & Longair, M. S. 1981, MNRAS, 194, 111
Hammer, F., & Le Fèvre, O. 1990, ApJ, 357, 38
Hewitt, A., & Burbidge, G. 1991, ApJS, 75, 297
Jenkins, C. J., Pooley, G. G., & Riley, J. M. 1977, MNRAS, 84, 61
Laing, R. A., Riley, J. M., & Longair, M. S. 1983, MNRAS, 204, 151
Laing, R. A. 1988, Nature, 331, 149
Laing, R. A. 1989, in Hot Spots in Extragalactic Radio Sources, edited by K. Meisenheimer and H.-J. Röser (Springer, Berlin), p. 27
Leahy, J. P. 1992, private communication
Leahy, J. P., Muxlow, T. W. B., & Stephens, P. W. 1989, MNRAS, 239, 401
Le Fèvre, O., Hammer, F., Nottale, L., & Mathez, G. 1987, Nature, 326, 268
McCarthy, P. J. 1988, Ph.D. thesis, University of California, Berkeley

McCarthy, P. J., van Breugel, W. J. M., Spinrad, H., & Djorgovski, S. 1987, ApJ, 321, L29
McCarthy, P. J., van Breugel, W. J. M., & Kapahi, V. K. 1991, ApJ, 371, 478
Pedelty, J. A., Rudnick, L., McCarthy, P. J., & Spinrad, H. 1989, AJ, 97, 647
Perley, R. A., Dreher, J. W., & Cowan, J. J. 1984, ApJ, 285, L35
Rigler, M. A., Lilly, S. J., Stockton, A., Hammer, F., & Le Fèvre, O. 1992, ApJ, 385, 61
Riley, J. M., Longair, M. S., & Gunn, J. E. 1980, MNRAS, 192, 233
Schilizzi, R. T., Kapahi, V. K., & Neff, S. G. 1982, A&A, 3, 173
Schwab, F. R. 1980, Proc. SPIE, 231, 18
Spinrad, H., Djorgovski, S., Marr, J., & Aguilar, L. 1985, PASP, 97, 932
Strom, R. G., & Conway, R. G. 1985, A&AS, 61, 547
Tabara, H., & Inoue, M. 1980, A&AS, 39, 379

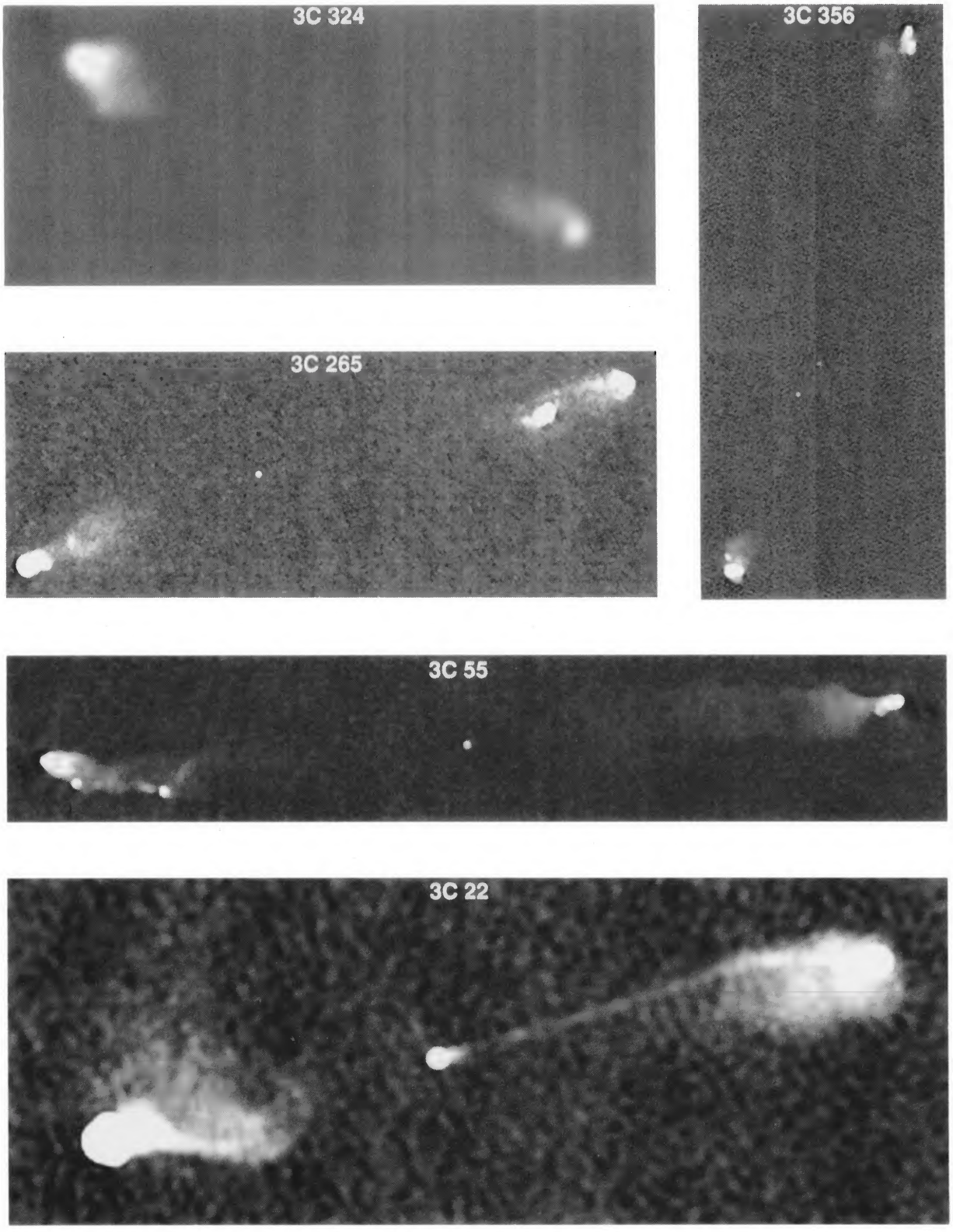


FIG. 1. Greyscale maps of 3C 22, 3C 55, 3C 265, 3C 324, and 3C 356.

Fernini *et al.* (see page 1693)